

Induced superconductivity in the fractional quantum Hall edge

Önder Gül^{1*}, Yuval Ronen^{1*}, Si Young Lee^{1,2*}, Hassan Shapourian^{1,3}, Jonathan Zauberman¹, Young Hee Lee^{2,4}, Kenji Watanabe⁵, Takashi Taniguchi⁶, Ashvin Vishwanath¹, Amir Yacoby¹, Philip Kim¹✉

Topological superconductors represent a phase of matter with nonlocal properties which cannot smoothly change from one phase to another, providing a robustness suitable for quantum computing^{1–5}. Substantial progress has been made towards a qubit based on Majorana modes^{6–15}, non-Abelian anyons of Ising (Z_2) topological order whose exchange—braiding—produces topologically protected logic operations. However, because braiding Ising anyons does not offer a universal quantum gate set, Majorana qubits are computationally limited⁴. This drawback can be overcome by introducing parafermions¹⁶, a novel generalized set of non-Abelian modes (Z_n), an array of which supports universal topological quantum computation^{17–19}. The primary route to synthesize parafermions involves inducing superconductivity in the fractional quantum Hall (fqH) edge^{18–23}. Here we use high-quality graphene-based van der Waals devices with narrow superconducting niobium nitride (NbN) electrodes, in which superconductivity and robust fqH coexist. We find crossed Andreev reflection (CAR) across the superconductor separating two counterpropagating fqH edges which demonstrates their superconducting pairing. Our observed CAR probability of the integer edges is insensitive to magnetic field, temperature, and filling, which provides evidence for spin-orbit coupling inherited from NbN enabling the pairing of the otherwise spin-polarized edges. FqH edges notably exhibit a CAR probability higher than that of integer edges once fully developed. This fqH CAR probability remains nonzero down to our lowest accessible temperature, suggesting superconducting pairing of fractional charges. These results provide a route to realize novel topological superconducting phases with universal braiding statistics in fqH–superconductor hybrid devices based on graphene and NbN.

A theoretical proposal⁵ to synthesize a topological superconductor from a topological insulator and a conventional (s-wave) superconductor has motivated hybrid approaches to realize Majorana modes. Besides topological insulators^{6–8}, these approaches now include spin-orbit coupled semiconductors^{9–14}, magnetic atom chains¹⁵, and integer quantum Hall edges^{24–26}—all in combination with a superconductor—offering either a testbed for or a route towards topological qubits. Common to all of these is the noninteracting description of charge carriers and Ising topological order which is insufficient for universal quantum computation⁴. These approaches, however, can be extended to the computationally universal Fibonacci order²⁷ predicted to emerge in a coupled parafermion array¹⁸.

Parafermions, unlike Majoranas, require electron–electron interactions to form, which result in richer non-Abelian braiding statistics¹⁶. An established condensed matter system that forms with interactions is the fqH state, which is the basis of different approaches for synthesizing parafermions^{17–23,27,28}. The primary approach—combining fqH, appearing in semiconductor heterostructures, with superconductivity^{18–23}—has so far presented two major experimental challenges. First, the strong magnetic fields required for fqH suppress superconductivity^{24–26,29}. Second, coupling a superconductor to a semiconductor heterostructure can be difficult, often leading to a nontransparent interface. Here, we overcome these challenges by using graphene-based van der Waals (vdW) heterostructures coupled to superconducting niobium nitride (NbN). The high device quality decreases the magnetic fields required for robust fqH to the regime where NbN remains superconducting owing to its large critical field. The superconductor edge–contact to graphene provides an interface transparent enough to induce superconductivity in quantum Hall edges.

Figure 1a shows the schematic of our vdW heterostructure, consisting of single-layer graphene as the conducting channel, which is first encapsulated by hexagonal boron nitride dielectric and then by graphite on both top and bottom. This heterostructure maximizes the channel mobility owing to the metallic graphite layers screening remote impurities^{30,31}, which is essential for reaching the fqH phase at magnetic fields low enough to allow

superconductivity. Figure 1b shows a typical device, including the heterostructure (purple) and a NbN superconductor (blue) which is sufficiently narrow (~ 100 nm) to ensure pairing between the fqH edges along both sides (Extended Data Figure 1). Such a superconducting pairing dramatically affects transport: when the injected electron-like charges are drained from the superconductor, hole-like charges propagate away (Figure 1c). This process—crossed Andreev reflection (CAR)—is the crucial ingredient for realizing parafermions³².

We have measured the resistance $R_{CAR} = V_{CAR}/I_{exc}$ as well as the Hall resistance $R_{XY} = V_{XY}/I_{exc}$ as a function of gate voltage (charge carrier density) at a magnetic field $B = 14$ T for different temperatures T (Figure 1d). Here, V_{CAR} is the potential of the edge propagating away from the grounded superconductor, V_{XY} the Hall voltage, and I_{exc} the bias current (see Figure 1b for the circuit). At low T , R_{CAR} becomes negative for quantized values of R_{XY} . We find an $R_{CAR} < 0$ for both integer fillings 1 and 2²⁵, and importantly for several fractional fillings 1/3, 2/5, 2/3, 5/3—our main finding (blow-up shown in Figure 1e). An $R_{CAR} < 0$ indicates that the electron-like carriers drained from the superconductor produce hole-like carriers with opposite charges, a direct result of crossed Andreev reflection, which reverses the sign of the edge potential. R_{CAR} acquires positive values either when R_{XY} is nonquantized and the bulk of the device conducts, or when superconductivity is suppressed with increasing T —both destroying CAR as expected. We confirm that our narrow NbN superconducts at 14 T for $T < 8$ K by measuring a strip with identical dimensions as the one coupled to the quantum Hall edges (Figure 1d inset). In a separate cooldown with T reaching 15 mK, we find $R_{CAR} < 0$ for several fractional fillings for a wide range of B (Figure 1f). At this low temperature, superconducting pairing of fqH edges can be observed in magnetic fields as low as 3 T (filling 2/3).

Figure 2a shows R_{CAR} with the accompanying longitudinal resistance R_{XX} as a function of filling ν . For all integer fillings R_{XX} , which measures bulk conduction, is much smaller in amplitude than R_{CAR} , linking R_{CAR} strictly to the potential of the edge leaving the superconductor. We find a negative edge potential with consistently increasing amplitude for lower fillings,

¹Department of Physics, Harvard University, Cambridge, MA, USA. ²Center for Integrated Nanostructure Physics (CINAP), Institute for Basic Science (IBS), Suwon, Republic of Korea. ³Department of Physics, Massachusetts Institute of Technology, Cambridge, MA, USA. ⁴Department of Energy Science, Sungkyunkwan University, Suwon, Republic of Korea. ⁵Research Center for Functional Materials, National Institute for Materials Science, Tsukuba, Japan. ⁶International Center for Materials Nanoarchitectonics, National Institute for Materials Science, Tsukuba, Japan. *These authors contributed equally: Önder Gül, Yuval Ronen, Si Young Lee. ✉e-mail: philipkim@g.harvard.edu

which remains negative for all integer ν and measured B demonstrating the robustness of CAR (Figure 2a inset).

The increasing amplitude of R_{CAR} with decreasing ν is connected to the decreasing number of edges, which increases R_{XY} . This dependence of R_{CAR} on ν can be understood by introducing $p_{\text{CAR}} = -V_{\text{CAR}}/V$, the probability of crossed Andreev reflection, where V is the potential of the incoming edge. The Hall voltage constrains $V_{\text{XY}} = V - V_{\text{CAR}}$, leading to the proportional relation $R_{\text{CAR}} = -R_{\text{XY}}/(1 + p_{\text{CAR}})$. This allows us to calculate p_{CAR} from the measured R_{CAR} , and thus to directly compare the CAR rate between different fillings. Figure 2b shows that p_{CAR} is comparable for all integer ν , including the spin-polarized $\nu=1$. This striking finding provides clear evidence for the presence of strong spin-orbit coupling (SOC) in the proximitized quantum Hall edges, which is inherited from the NbN superconductor. Without this induced SOC, spin-polarized edges cannot pair due to the s-wave superconducting pairing in NbN. Our calculated Bogoliubov-de Gennes spectrum confirms this observation (Extended Data Figure 2; see Figure 2b inset and Methods for the theory model). Figure 2c and d show the energy spectrum of $\nu=1$ and 2 without and with SOC, represented in our Hamiltonian by the term λ_{R} . A pairing gap Δ_{ind} does not open without SOC (Figure 2c). The inclusion of SOC induces pairing ($\Delta_{\text{ind}} > 0$) between the two counterpropagating spin-up edges of $\nu=1$, and separately between the two additional counterpropagating spin-down edges of $\nu=2$ (Figure 2d)—pairing between the edges with opposite spin polarization is forbidden owing to the difference in their Fermi wave vector k_{F} . This necessarily implies that our induced superconducting gap Δ_{ind} is topologically nontrivial for all integer ν , consistent with the observed magnetic-field-insensitive p_{CAR} for small I_{exc} and T compared to Δ_{ind} .

A topological Δ_{ind} is predicted to result in $p_{\text{CAR}}=1$, known as quantized Majorana conductance³³. However, our p_{CAR} remains much smaller than unity. We account for this in our model by introducing a parameter Z to represent various processes which lead to the tunneling of incoming charges to outgoing edges without Andreev reflection (Figure 2b inset), analogous to that in Blonder-Tinkham-Klapwijk formalism³⁴. Cotunneling and quasiparticle transport due to vortices are the leading effective mechanisms contributing to Z . From the measured p_{CAR} we extract $Z \sim 0.45$ which is constant for all integer ν . Our model does not include mode-mixing or edge reconstruction³⁵ at the superconductor interface, both expected to be relevant in our device. However, it confirms that transport via Andreev edge states, demonstrated in quantum Hall–superconductor hybrids^{24,26,29}, cannot result in a pairing gap or a robust $R_{\text{CAR}} < 0$, excluding this mechanism for our observations (Extended Data Figure 15).

We now extend our analysis of p_{CAR} to fractional ν and a larger B range. Figure 3a shows p_{CAR} and the accompanying νR_{XX} (R_{XX} normalized for different ν), with the measured R_{CAR} and R_{XX} at $B=9$ T plotted in Figure 3b. For all fractional ν with induced pairing ($R_{\text{CAR}} < 0$), we find a negligibly small R_{XX} which excludes bulk conduction. Bulk conduction does, however, result in $R_{\text{CAR}} > 0$ observed for lower values of B or for fractional ν with smaller excitation gaps. Figure 3c shows the B dependence of p_{CAR} for several fractional and integer ν along with the expected p_{CAR} for our Z . In this B range, we again find for several fillings a p_{CAR} that does not depend on B and is comparable between different ν , this time including several fractional ν (Figure 3b inset). However, this observation is contrasted by $\nu=1/3$ and $4/3$, which present well-developed fqH (negligible R_{XX}) together with a strong magnetic field dependence. This behavior can be either intrinsic to the superconducting pairing of fqH edges or a result of a B -dependent Z for certain fractional fillings. Identifying either of these scenarios theoretically is challenging due to the complex (interacting many-body) nature of fqH. Experimentally, we find a p_{CAR} that strongly depends on B (and T , discussed below) only for the fqH states whose p_{CAR} is significantly larger than that for integer ν . Such B and T dependencies are much weaker for the fqH states in our

second device—albeit with a slightly different geometry measured at $T > 1.75$ K—for which p_{CAR} is comparable for both integer and fractional ν (Extended Data Figure 3-9).

Next, we perform spectroscopy on our fqH–superconductor hybrid. By tuning V , serving as bias voltage (Figure 1b), we have varied the energy of the injected charges and monitored p_{CAR} and R_{XX} simultaneously at different temperatures, shown in Figure 4a-d for $\nu=1/3$ and $2/5$. We find CAR to be limited to an energy range below $|eV| \sim 1$ meV and to low T (see also the color plots as insets and Extended Data Figure 10 which shows R_{CAR} instead of p_{CAR}). Increasing V and T bring the injected charges above the excitation gap of the fractional fillings (bulk conduction) or above Δ_{ind} (Bogoliubov-quasiparticle transport without Andreev reflection), both suppressing CAR.

To distinguish whether an increasing V and T suppress CAR due to bulk conduction or quasiparticle transport, we compare fractional ν with $\nu=2$ which has the largest Landau gap. While the excitation gaps for fractional ν are in the same range as Δ_{ind} , the energy gap of $\nu=2$ is significantly larger, allowing us to deduce the suppression mechanism. First, the left inset of Figure 4a shows CAR for a larger range of V at $\nu=2$ compared to $\nu=1/3$ and $2/5$ (Figure 4a, c). Second, Figure 4b and d show that for fractional ν , R_{XX} (bulk conduction) increases even for a small increase of V . Finally, Extended Data Figure 9 shows that for $\nu=2$, R_{XX} remains negligibly small with increasing T despite vanishing p_{CAR} . Based on these observations, we conclude that for our fractional ν an increasing V suppresses CAR primarily due to bulk conduction, while the suppression with T is due to both bulk conduction and Bogoliubov-quasiparticle transport.

We proceed with the temperature dependence of p_{CAR} for several integer and fractional ν (Figure 4e). We find consistent CAR below ~ 5 K for all well-developed fillings, demonstrating the robustness of the induced superconductivity. Above this T increasing quasiparticle transport overcomes CAR. The CAR at $\nu=1$ and 2 persists up to a larger T in our second device measured using a different setup (Extended Data Figure 9), indicating that quasiparticle transport—an outstanding challenge for topological qubits—can be further decreased.

Figure 4f shows the vertical cuts from Figure 4e for several ν . We find a p_{CAR} saturating at low temperatures for the integer fillings $\nu=1, 2$ as well as $\nu=2/3$. This temperature independence of integer ν is consistent with our topological Δ_{ind} , equivalent to the B independence presented in Figure 2 and 3. In contrast, $\nu=1/3$ and $2/5$ show a clear temperature dependence down to the lowest T (Extended Data Figure 11), with the p_{CAR} of $\nu=1/3$ reaching above 6% at $T=15$ mK as shown in Figure 3 ($B=9$ T).

An increasing p_{CAR} with decreasing T is a distinctive feature of the superconducting pairing of fractional charges e^* (Figure 4f right inset and Extended Data Figure 21). Here, CAR converts an incoming electron-like $e^*=1/3$ to an outgoing hole-like $-e^*=-1/3$ adding a $2/3$ charge to the superconductor, a mechanism which strictly requires the presence of parafermions¹⁶. Such T dependence is not compatible with the alternative scenario of pairing of integer charges (Figure 4f left inset), where three incoming e^* bunch together, which are then converted to three bunched $-e^*$ leaving the superconductor. In this case, CAR vanishes ($R_{\text{CAR}}=0$) at zero temperature which is not observed for both our devices at our lowest T . Our p_{CAR} for fully developed fqH states being larger than that of integer ν further suggests different underlying mechanisms for CAR in fractional and integer ν .

Our presented experiments show induced superconductivity in the fractional quantum Hall edge, with the pairing enabled by spin-orbit coupling inherited from the superconductor. This result demonstrates all the known required ingredients for parafermions. Following experiments, including tunneling^{28,36} and noise measurements³⁷, will be able to reveal spectroscopic and nonlocal signatures of parafermions in this fqH–superconductor hybrid system.

1. Kitaev, A. Y. Fault-tolerant quantum computation by anyons. *Ann. Phys.* **303**, 2–30 (2003).
2. Read, N. & Green, D. Paired states of fermions in two dimensions with breaking of parity and time-reversal symmetries and the fractional quantum Hall effect. *Phys. Rev. B* **61**, 10267 (2000).
3. Kitaev, A. Y. Unpaired Majorana fermions in quantum wires. *Phys.-Uspekhi* **44**, 131–136 (2001).
4. Nayak, C., Simon, S. H., Stern, A., Freedman, M. & Das Sarma, S. Non-Abelian anyons and topological quantum computation. *Rev. Mod. Phys.* **80**, 1083 (2008).
5. Fu, L. & Kane, C. L. Superconducting proximity effect and Majorana fermions at the surface of a topological insulator. *Phys. Rev. Lett.* **100**, 096407 (2008).
6. Hart, S. *et al.* Induced superconductivity in the quantum spin Hall edge. *Nat. Phys.* **10**, 638–643 (2014).
7. Wiedenmann, J. *et al.* 4π -periodic Josephson supercurrent in HgTe-based topological Josephson junctions. *Nat. Commun.* **7**, 10303 (2016).
8. Sun, H.-H. *et al.* Majorana zero mode detected with spin selective Andreev reflection in the vortex of a topological superconductor. *Phys. Rev. Lett.* **116**, 257003 (2016).
9. Mourik, V. *et al.* Signatures of Majorana fermions in hybrid superconductor-semiconductor nanowire devices. *Science* **336**, 1003–1007 (2012).
10. Rokhinson, L. P., Liu, X. & Furdyna, J. K. The fractional a.c. Josephson effect in a semiconductor–superconductor nanowire as a signature of Majorana particles. *Nat. Phys.* **8**, 795–799 (2012).
11. Das, A. *et al.* Zero-bias peaks and splitting in an Al–InAs nanowire topological superconductor as a signature of Majorana fermions. *Nat. Phys.* **8**, 887–895 (2012).
12. Deng, M. T. *et al.* Anomalous zero-bias conductance peak in a Nb–InSb nanowire–Nb hybrid device. *Nano Lett.* **12**, 6414–6419 (2012).
13. Finck, A. D. K., Van Harlingen, D. J., Mohseni, P. K., Jung, K. & Li, X. Anomalous modulation of a zero-bias peak in a hybrid nanowire-superconductor device. *Phys. Rev. Lett.* **110**, 126406 (2013).
14. Churchill, H. O. H. *et al.* Superconductor-nanowire devices from tunneling to the multichannel regime: Zero-bias oscillations and magnetoconductance crossover. *Phys. Rev. B* **87**, 241401 (2013).
15. Nadj-Perge, S. *et al.* Observation of Majorana fermions in ferromagnetic atomic chains on a superconductor. *Science* **346**, 602–607 (2014).
16. Alicea, J. & Fendley, P. Topological phases with parafermions: theory and blueprints. *Annu. Rev. Condens. Matter Phys.* **7**, 119–139 (2016).
17. Vaezi, A. & Barkeshli, M. Fibonacci anyons from Abelian bilayer quantum Hall states. *Phys. Rev. Lett.* **113**, 236804 (2014).
18. Mong, R. S. K. *et al.* Universal topological quantum computation from a superconductor-Abelian quantum Hall heterostructure. *Phys. Rev. X* **4**, 011036 (2014).
19. Vaezi, A. Superconducting Analogue of the parafermion fractional quantum Hall states. *Phys. Rev. X* **4**, 031009 (2014).
20. Clarke, D. J., Alicea, J. & Shtengel, K. Exotic non-Abelian anyons from conventional fractional quantum Hall states. *Nat. Commun.* **4**, 1348 (2013).
21. Lindner, N. H., Berg, E., Refael, G. & Stern, A. Fractionalizing Majorana fermions: non-Abelian statistics on the edges of Abelian quantum Hall states. *Phys. Rev. X* **2**, 041002 (2012).
22. Cheng, M. Superconducting proximity effect on the edge of fractional topological insulators. *Phys. Rev. B* **86**, 195126 (2012).
23. Vaezi, A. Fractional topological superconductor with fractionalized Majorana fermions. *Phys. Rev. B* **87**, 035132 (2013).
24. Amet, F. *et al.* Supercurrent in the quantum Hall regime. *Science* **352**, 966–969 (2016).
25. Lee, G.-H. *et al.* Inducing superconducting correlation in quantum Hall edge states. *Nat. Phys.* **13**, 693–698 (2017).
26. Zhao, L. *et al.* Interference of chiral Andreev edge states. *Nat. Phys.* **16**, 862–867 (2020).
27. Read, N. & Rezayi, E. Beyond paired quantum Hall states: Parafermions and incompressible states in the first excited Landau level. *Phys. Rev. B* **59**, 8084 (1999).
28. Barkeshli, M. & Qi, X.-L. Synthetic topological qubits in conventional bilayer quantum Hall systems. *Phys. Rev. X* **4**, 041035 (2014).
29. Rickhaus, P., Weiss, M., Marot, L. & Schönenberger, C. Quantum Hall effect in graphene with superconducting electrodes. *Nano Lett.* **12**, 1942–1945 (2012).
30. Zibrov, A. A. *et al.* Tunable interacting composite fermion phases in a half-filled bilayer-graphene Landau level. *Nature* **549**, 360–364 (2017).
31. Li, J. I. A. *et al.* Even-denominator fractional quantum Hall states in bilayer graphene. *Science* **358**, 648–652 (2017).
32. Clarke, D. J., Alicea, J. & Shtengel, K. Exotic circuit elements from zero-modes in hybrid superconductor–quantum-Hall systems. *Nat. Phys.* **10**, 877–882 (2014).
33. Law, K. T., Lee, P. A. & Ng, T. K. Majorana fermion induced resonant Andreev reflection. *Phys. Rev. Lett.* **103**, 237001 (2009).
34. Blonder, G. E., Tinkham, M. & Klapwijk, T. M. Transition from metallic to tunneling regimes in superconducting microconstrictions: Excess current, charge imbalance, and supercurrent conversion. *Phys. Rev. B* **25**, 4515 (1982).
35. Marguerite, A. *et al.* Imaging work and dissipation in the quantum Hall state in graphene. *Nature* **575**, 628–633 (2019).
36. Barkeshli, M., Oreg, Y. & Qi, X.-L. Experimental proposal to detect topological ground state degeneracy. Preprint at <https://arxiv.org/abs/1401.3750> (2014).
37. Schiller, N., Cornfeld, E., Berg, E. & Oreg, Y. Predicted signatures of topological superconductivity and parafermion zero modes in fractional quantum Hall edges. *Phys. Rev. Res.* **2**, 023296 (2020).

Methods

Assembly of the heterostructure We assembled our five-layer graphite/hexagonal boron nitride (hBN)/single layer graphene/hBN/graphite van der Waals heterostructures with the standard dry transfer technique³⁸, using a polycarbonate (PC)/polydimethylsiloxane (PDMS) stamp. We exfoliated the flakes via thermal release tape onto (doped) Si substrates covered with 285-nm-thick SiO₂—the same substrate on which the devices were fabricated. To increase the size of the flakes we baked the substrates, the tape carrying bulk hBN and graphite still adhered, at 100°C for 1 min on a hot plate before releasing the tape. After exfoliation we annealed the substrates with the flakes at high vacuum ($\sim 3 \cdot 10^{-7}$ mbar) and 350°C for 20 min to remove the tape residues, ramping the temperature from 20°C over three hours. We did not perform these two heat treatments on single-layer graphene to avoid modifying its intrinsic properties. We determined the cleanliness and thickness of the flakes by first optical and then atomic force microscopy. The graphite layers in our heterostructures were determined to be $\sim 1.5 - 3$ nm thick (5 to 10 layers) while the hBN layers were ~ 50 nm (top) and 90 - 100 nm (bottom), all confirmed to be atomically flat. We used a thicker bottom hBN to prevent an electrical connection between the bottom graphite and the overlapping superconductor (see Nanofabrication). After choosing suitable flakes, we assembled the heterostructure in a glove-box (H₂O < 0.1 ppm, O₂ < 0.1 ppm) to decrease contamination between the layers.

To make the stamp, we prepared a PC solution (8 wt.%) and pipetted it onto a glass slide. We placed another glass slide on top of the solution and left the resulting film to cure in ambient conditions. We then placed a rectangular block ($\sim 8 \times 5$ mm) of PDMS (Gel-Pak) on a separate glass slide and transferred the PC film (with a larger area than that of the PDMS) on top. To ensure adhesion between the PC film and the glass slide we baked the stamp at 180°C for 5 mins, and then mounted the finished stamp on a dry transfer setup.

Before transferring flakes, we flattened the surface of the PC film by touching the stamp onto a bare substrate held by vacuum on a sample stage at 155°C. After a cooldown period during which the PC film detached from the bare substrate, we replaced the substrate with the one containing the top graphite. The stamp was used to pick up the graphite at $\sim 130^\circ\text{C}$, followed by a cooldown until the stamp detached. We then used this top graphite to pick up the top hBN via van der Waals force. In this step, the top graphite approached the hBN extremely slowly at 150 - 155°C to minimize the formation of bubbles. We picked up this hBN, the graphene, and the bottom hBN with the same procedure described above. We then dropped the whole stack (graphite/hBN/graphene/hBN) from the stamp onto the bottom graphite at $\sim 170^\circ\text{C}$. Importantly, dropping the stack at this high-temperature allowed us to push out the bubbles formed between the layers during assembly³⁹. Finally, we released the PC film at 190°C, ending the transfer process. We completed the assembly by removing polymer residues from the heterostructure, first leaving the chip in chloroform overnight and then annealing the heterostructure at high vacuum ($\sim 3 \cdot 10^{-7}$ mbar) and 350°C for 30 minutes after a 3 hour temperature ramp.

Nanofabrication We defined the superconductor, normal leads, and the shape of the device via electron beam lithography followed by reactive ion etching (RIE). For RIE, we used a CHF₃, Ar, and O₂ gas mixture, whereas we excluded CHF₃ for the selective removal of the top graphite. Both the superconductor and the normal leads contact the graphene from its edge, and were deposited following RIE in one lithography step in which the etch mask also served as the deposition mask. For the superconductor, we first selectively etched the top graphite that would otherwise surround the superconductor, leaving a ~ 100 nm separation to avoid an electrical connection. In the subsequent lithography step, we deposited the superconductor

after vertically etching the heterostructure beyond the graphene layer using an etch-stop. This etch-stop is based on the ex-situ measured conductance of a test area of identical layer composition, and leaves most of the bottom hBN unetched which insulates the superconductor from the bottom graphite. Unlike the superconductor, the normal leads do not overlap the top or bottom graphite, and instead connect to the fractional quantum Hall heterostructure through graphene that extends beyond both graphite layers (Extended Data Figure 1).

The normal leads are Cr/Pd/Au (2/7/150 nm), thermally evaporated on a rotating sample stage with $\sim 15^\circ$ tilt. We deposited our superconductor in an AJA International UHV hybrid system (base pressure $\sim 10^{-7}$ Torr). The superconductor deposition started with electron beam evaporation of Ti (10 nm, with rotation and 30° tilt) immediately followed by dc magnetron sputtering of Nb/NbN (5/75 nm, without tilt) at a pressure of 3 mTorr and a power of 200 W using a Nb target. We deposited Nb in an Ar environment. For NbN we used an Ar/N₂ (50/6 sccm) gas mixture. This superconductor has a critical temperature $T_c \sim 12$ K at $B=0$ T.

Measurement The parts of the graphene that extend beyond the top and bottom graphite, which connect the normal leads to the fractional quantum Hall heterostructure, were doped by using the substrate as a global gate. The top and bottom graphite layers were used as gates to control the charge carrier density in the fractional quantum Hall heterostructure. Device 1 used top graphite as the gate while the bottom graphite was grounded, whereas the opposite was the case for Device 2.

We measured Device 1 in a variable temperature inset (VTI) at $T \geq 1.75$ K and in a dilution refrigerator with its cold finger at $T = 15$ mK, and Device 2 in a different VTI at $T \geq 1.6$ K. For the measurements in VTIs, we used an RC filter attached to the chip carrier, whereas the dilution refrigerator was equipped with RC, copper powder and pi filters all thermalized to the cold finger. We reproduced our observations after every thermocycle for both our devices. Importantly, however, we were unable to measure crossed Andreev reflection without a filter.

We used the standard ac lock-in technique ($f < 100$ Hz) with an excitation current $I_{exc} = 5$ or 10 nA for the VTI measurements and $I_{exc} = 1$ or 5 nA for the dilution refrigerator measurements. All presented measurements used a single source and the superconductor as the single drain. Because of the finite resistance (wiring and filters) between the superconductor and the breakout box at room temperature, V_{CAR} and V (Figure 1b) were measured relative to the superconductor potential. Our superconductor coupled to the fractional quantum Hall edges branches out to four separate leads (Extended Data Figure 1). Two branch out immediately after leaving the heterostructure (one used as the drain, the other to monitor the potential), and the remaining two (left floating) after a narrow strip with identical dimensions as the one coupled to the fractional quantum Hall edges. This strip allowed for an independent test of our superconductor.

Theory The inset of Figure 2b shows the schematic of the vertically shrunk experimental system which satisfies $I_{exc} = \nu \cdot e^2/h \cdot (V - V_{CAR})$. A $p_{CAR} = 1$ implies $R_{CAR}/R_{XY} = -1/2$. In what follows, we present a low energy theory of graphene in the presence of a strong out-of-plane B^{40} (Extended Data Figure 12) and compute the crossed Andreev reflection for integer fillings. We put the system on a cylinder and choose the Landau gauge to preserve translation invariance along the compactified direction (y -axis). This choice is for convenience in our calculations and does not affect the spectral properties or the response functions.

We encapsulate the slowly varying field operators in an eight-component field and introduce the Pauli matrices s_α , τ_α and σ_α which act on spin, valley and sublattice degrees of freedom, respectively. In this notation, the Hamiltonian reads $H_0 = \int d^2x \psi^\dagger(\mathbf{r}) h_0 \psi(\mathbf{r})$ where

$h_0 = v_F(-i\hbar\partial_x - eA_x)\tau_z\sigma_x + v_F(-i\hbar\partial_y - eA_y)\sigma_y + m\sigma_z - \mu + g s_z$ with the chemical potential μ , the Zeeman term g , and a Dirac mass term m (necessary to realize $\nu = 1$ in our noninteracting analysis). The energy levels are given by $\varepsilon_n = \sqrt{|n|\varepsilon_0^2 + m^2} \pm g$ where n is integer and $\varepsilon_0 = \sqrt{2e\hbar B}v_F$ is the characteristic energy scale of the Landau level spacing for the Dirac Hamiltonian. We model the superconducting region with the pairing terms^{41,42} $\psi_\dagger[\Delta_1\tau_x + \Delta_2\tau_0]\psi_\downarrow$. Both pairing terms are of spin-singlet s -wave type, with the first term describing an inter-valley pairing, and the second term an intra-valley pairing. The inter-valley pairing (first term) does not result in a gap when interfaced with an s -wave superconductor so whether it is singlet or triplet in the valley basis is irrelevant. The intra-valley pairing (second term), on the other hand, is essential for gap opening and present only for the interface along the armchair edge. Therefore, we limit our analysis to an armchair edge (interface along y).

To find the energy spectrum at the interface between qH and a superconducting region, we solve the Bogoliubov-de Gennes (BdG) equation in the plane-wave basis $e^{i2\pi kx/W}$ where W is the length of the cylinder and $k = 0, \pm 1, \pm 2, \dots$ with a momentum cut-off $|k| < N_x$. Extended Data Figure 13 shows a typical energy spectrum near the edge for such interface. Here we set $g = 0$ and the bands are doubly degenerate due to spin rotation symmetry⁴³.

We now consider the counterpropagating edge modes along either side of the superconductor (Figure 2b inset, y -axis is along the superconductor). For reference, we show in Extended Data Figure 14 the armchair edge energy spectra in the absence and presence of the Dirac mass term, where we replace the superconducting region with vacuum. Without any (valley) symmetry breaking, the quantum Hall sequence is $\nu = 2, 4, 6, \dots$. Adding the Dirac mass term modifies the sequence into $\nu = 1, 2, 4, \dots$ with a spin and valley polarized $\nu = 1$. Turning on superconductivity yields Extended Data Figure 15, with the top panels for $\nu = 1$ and the bottom panels for $\nu = 2$. For any integer filling zero-energy band crossings are between particle-hole partners with identical spin polarization. Therefore, there is no direct mechanism for s -wave pairing (even for spin-unpolarized fillings such as $\nu = 2$). However, the large spin-orbit coupling in NbN superconductor provides a necessary ingredient for a spin-flip process allowing for a pairing between electrons with the same spin polarization. We account for spin-orbit coupling via⁴⁴

$$h_{so} = \lambda_{so}\tau_z s_z \sigma_z + \lambda_{R,x}\tau_z s_y \sigma_x - \lambda_{R,y}s_x \sigma_y.$$

Because the induced pairing between the counterpropagating edge modes exponentially decays as a function of the superconductor thickness, a gap does not open for a thick superconductor (left panels). This is the experimental scenario in which Andreev edge states govern the transport^{24,26,29}. Reducing the thickness of the superconductor hybridizes the edge modes along both sides of the superconductor and opens a gap in the BdG spectrum (middle panels). The band crossings and the resulting hybridization occur for each mode separately—each edge mode (for instance spin-up and spin-down) experiences a similar induced pairing (gap opening) mechanism. The gap opening term is a spin-polarized pairing of the form $\psi_{Ls}\psi_{Rs}$ which originates from the combination of the spin-singlet pairing of the parent superconductor and spin-orbit coupling. Turning off spin-orbit coupling results in zero-energy band crossings remaining intact (right panels). The degeneracy points (band crossings at finite energies) near $k_y = 0$ are lifted for a thin superconductor regardless of the presence of spin-orbit coupling. This is because those degeneracies open by either spin-singlet intra-edge pairing or simply direct tunneling. Nevertheless, these processes do not play any role for the zero-energy band crossings between two spin-polarized modes, because the former process does not open a gap in a spin-polarized channel and the latter is forbidden at finite k due to violating the momentum conservation. This implies that $\nu = 2$

edge modes can be treated effectively as two copies of $\nu = 1$. Our numerical analysis confirms that the induced gaps within different edge modes are of the same order and decrease as the superconductor is made thicker (Extended Data Figure 16).

We now proceed to computing the probability of crossed Andreev reflection, a process which we effectively treat as a quasi-1D scattering problem of a superconducting region of width W_s sandwiched between two quantum Hall regions each with a width W (Figure 2b inset, superconductor along y). We first find the transfer operator of Dirac-BdG equation, which is the solution to the wave equation in the Nambu basis

$$\hbar v_F \frac{\partial \Psi_y(x)}{\partial y} = i\eta_z \sigma_y [E - h_0(x) - h_{sc} \theta(x)] \Psi_y(x). \quad (1)$$

Here, h_0 is the Hamiltonian intrinsic to the qH region

$$h_0(x) = v_F(-i\partial_x)\tau_z\sigma_x + ev_F A_y(x)\sigma_y + \eta_z(m(x)\sigma_z - \mu(x) + g(x)s_z),$$

h_{sc} the Hamiltonian of the superconducting region

$$h_{sc} = \Delta_1\eta_y\tau_x s_y + \Delta_2\eta_y s_y + \lambda_{so}\eta_z\tau_z s_z \sigma_z + \lambda_{R,x}\tau_z s_y \sigma_x - \lambda_{R,y}s_x \sigma_y,$$

η_α the Pauli matrices acting in the particle-hole subspace, $\theta(x)$ a box function nonzero only in the superconductor region, and $A_y(x)$ the gauge field

$$A_y(x) = \begin{cases} B(x - W_s/2) & x > +W_s/2 \\ B(x + W_s/2) & x < -W_s/2 \\ 0 & |x| \leq +W_s/2 \end{cases}$$

chosen such that the magnetic field vanishes inside the superconductor. The Dirac mass term, local chemical potential, and the Zeeman term are

$$m(x) = \begin{cases} m_s & |x| \leq W_s/2 \\ m_n & |x| > W_s/2 \end{cases} \quad \mu(x) = \begin{cases} \mu_s & |x| \leq W_s/2 \\ \mu_n & |x| > W_s/2 \end{cases} \\ g(x) = \begin{cases} g_s & |x| \leq W_s/2 \\ g_n & |x| > W_s/2. \end{cases}$$

We neglect the Zeeman term in the superconductor for simplicity. We set $\mu_{sc} = 8\varepsilon_0$ and $m_{sc} = 3\varepsilon_0$ to model a superconductor with quadratic bands.

We now solve equation (1) in a plane-wave basis representation where the basis vectors are given by

$$\psi_{ek}^\pm = \frac{1}{\sqrt{W_t}} e^{iq_k x} |+_z\rangle_\eta | \pm_y \rangle_{\sigma'}, \quad \psi_{hk}^\pm = \frac{1}{\sqrt{W_t}} e^{iq_k x} |-_z\rangle_\eta | \mp_y \rangle_{\sigma'}, \quad q_k = \frac{2\pi k}{W_t},$$

where $W_t = 2W + W_s$ is the total width of the system, $| \pm_y \rangle_{\sigma'}$ denote eigenstates of σ_y , that is, $\sigma_y | \pm_y \rangle_{\sigma'} = \pm | \pm_y \rangle_{\sigma'}$ and $| \pm_z \rangle_\eta$ denote particle (hole) states, that is, $\eta_z | \pm_z \rangle_\eta = \pm | \pm_z \rangle_\eta$ (recall $\eta_z \equiv 2\psi^\dagger\psi - 1$). We put the subscript e and h to emphasize the distinction between the particle and hole states. We omitted the explicit writing of spin/valley basis vectors in the states above for brevity since the kinetic term in y direction is diagonal in these subspaces. The final quantities involve summations over both spin and valley degrees of freedom. The reflection matrix r is then determined by matching the amplitudes of incoming, reflected, and transmitted modes at $y = 0$,

$$\sum_k [\delta_{kk'} \psi_{ek}^+(x) + r_{kk'}^h \psi_{hk}^-(x) + r_{kk'}^e \psi_{ek}^-(x)] = \Psi_0(x)$$

where $\Psi_0(x)$ only contains forward propagating and decaying evanescent wave solutions to equation (1).

To get the scattering of an incoming electron from the upper qH plane $x > W_s/2$ to a hole in the lower half plane $x < -W_s/2$, we compute the collective probability of crossed Andreev reflection $P_n = Tr(r_n^\dagger X r_n X^*)$ (note $0 \leq P_n \leq \nu$), where X matrix is the unitary matrix transforming q_k -modes to real-space modes $X_{kk'} = \int_0^W e^{i2\pi(k-k')(x+W_s/2)/W_t} dx$. Left panel of Extended Data Figure 17 shows the collective crossed Andreev reflection probability as a function of the chemical potential in the qH region. The plateaus correspond to different integer qH states in the normal region and the quantization is because of gap opening in the spectrum which effectively gives rise to ν copies of topological superconductors at a filling ν . We also plotted the bias dependence at two values of chemical potential which represent filling $\nu = 1$ and 2. It is interesting to note that there is a second plateau for $\nu = 2$ at finite bias which corresponds to gap opening between opposite spin species (similar to ordinary Andreev reflection).

Effective edge theory: We now proceed with effective theories at $\nu = 1$ and 2 edges for a more quantitative understanding. For simplicity, we start with $\nu = 1$ and derive a minimal model which reproduces the BdG spectrum in Extended Data Figure 15. To derive an ansatz for nonlinear conductance $G = I_{exc}/V$, we first reduce the problem to a 1D scattering between two sets of edge modes, as shown in inset of Figure 2b. We begin with the effective Hamiltonian

$$H_0 = v_F \int dy [\psi_R^\dagger(y)(-i\partial_y - k_0)\psi_R(y) + \psi_L^\dagger(y)(i\partial_y - k_0)\psi_L(y)],$$

where we introduce two Fermi fields ψ_L and ψ_R to describe the edge modes near the upper and lower voltage probes. R and L refer to the right/left movers. We take into account the proximity effect of superconductor via the following terms

$$\Delta \psi_R \psi_L + \sum_{\sigma=L,R} \tilde{\Delta} \psi_\sigma (-i\partial_y) \psi_\sigma + \text{H.c.}$$

where Δ and $\tilde{\Delta}$ are two phenomenological constants to model the inter-edge and intra-edge pairing, respectively.

It is more convenient to rewrite the full Hamiltonian in the Nambu basis $\Psi^\dagger = (\psi_R^\dagger, \psi_L^\dagger, \psi_R, \psi_L)$. The problem is then mapped to a single-particle BdG equation $\mathcal{H}|\Psi\rangle = E|\Psi\rangle$,

$$\mathcal{H} = v_F(-i\partial_y)\sigma_z - v_F k_0 \tau_z + \Delta \tau_y \sigma_y + \tilde{\Delta}(-i\partial_y)\tau_x$$

where τ_α and σ_α are Pauli matrices acting on particle-hole and left/right mover degrees of freedom, respectively. This Hamiltonian is particle-hole symmetric, that is, it satisfies the identity $U\mathcal{H}^T U^\dagger = -\mathcal{H}$ where $U = \tau^x$, and belongs to topological phases of the symmetry class D in the noninteracting classification⁴⁵⁻⁴⁷. The Bogoliubov spectrum associated with this Hamiltonian is given by

$$\epsilon_q = \pm \sqrt{\left(v_F q \pm \sqrt{\tilde{\Delta}^2 q^2 + v_F^2 k_0^2}\right)^2 + \Delta^2},$$

which is shown in Extended Data Figure 18. The intra-edge term modifies the velocity of the modes $v_F \rightarrow v_F \pm \tilde{\Delta}$. However, crossed Andreev reflection (discussed below) does not depend on this effect.

For simplicity, we assume that the superconductor is infinitely long. We consider the interface to be at $y = 0$, so that

$$\Delta(y) = \begin{cases} \Delta & y > 0 \\ 0 & y < 0. \end{cases}$$

We consider the following ansatz for the wave function in the two regions:

$$\begin{aligned} \Psi(y) &= A_1 \Psi_{ke}^{(R)}(y) + A_2 \Psi_{kh}^{(R)}(y) + B_1 \Psi_{ke}^{(L)}(y) + B_2 \Psi_{kh}^{(L)}(y) & y < 0 \\ \Psi(y) &= C_1 \Psi_{q+}^{(R)}(y) + C_2 \Psi_{q-}^{(R)}(y) + D_1 \Psi_{q+}^{(L)}(y) + D_2 \Psi_{q-}^{(L)}(y) & y > 0, \end{aligned}$$

where the superscript (R) or (L) refer to the right or left movers, respectively, and \hbar and e denote the electron and hole degrees of freedom.

To find the scattering matrix elements, we find the transfer matrix by demanding the wave function to be continuous at the interface $y = 0$:

$$\begin{pmatrix} C \\ D \end{pmatrix} = \begin{pmatrix} T_{RR} & T_{RL} \\ T_{LR} & T_{LL} \end{pmatrix} \begin{pmatrix} A \\ B \end{pmatrix}, \quad (2)$$

where T_{ij} are 2×2 matrices in particle-hole basis and the subscripts denote the transfer of right/left mover to left/right mover from $y < 0$ region to $y > 0$ region. We also multiply it by another transfer matrix to account for various processes such as electrons bypassing the superconductor (shown by the arrow in Figure 2b inset) or possible chemical potential or velocity mismatch⁴⁸ between incoming modes and hybridized modes,

$$T^{(z)} = \begin{pmatrix} 1 - iZ & 0 & -iZ & 0 \\ 0 & 1 + iZ & 0 & -iZ \\ iZ & 0 & 1 + iZ & 0 \\ 0 & iZ & 0 & 1 - iZ \end{pmatrix},$$

which is parametrized by Z as follows: $Z = 0$ and $Z \rightarrow \infty$ correspond to no tunneling (perfect junction with the proximitized modes) and perfect tunneling (fully detached from the proximitized modes), respectively.

From the above relation, we can read off the scattering matrix for an incoming wave such as

$$\Psi_{in}^e(y) = \frac{1}{\sqrt{2\pi v_F}} \begin{pmatrix} |+\rangle \\ 0 \end{pmatrix} e^{ik_e y},$$

which corresponds to

$$A = \begin{pmatrix} 1 \\ 0 \end{pmatrix}, \quad B = \begin{pmatrix} r_{ee} \\ r_{he} \end{pmatrix}, \quad C = \begin{pmatrix} t_{ee} \\ t_{he} \end{pmatrix}, \quad D = \begin{pmatrix} 0 \\ 0 \end{pmatrix}.$$

The reflection coefficients can then be found by eliminating C from equation (2),

$$B = \begin{pmatrix} r_{ee} \\ r_{he} \end{pmatrix} = -T_{LL}^{-1} T_{LR} \begin{pmatrix} 1 \\ 0 \end{pmatrix}.$$

In the clean limit, we exactly recover the Blonder-Tinkham-Klapwijk (BTK) formulas³⁴. In the zero-bias limit $E = 0$ and for arbitrary Z , we have

$$r_{ee} = -\frac{2Z(Z+i)}{2Z^2+1}, \quad r_{he} = \frac{i}{2Z^2+1},$$

which are independent of Δ .

To model a realistic system, we consider random pairing terms

$$V_{dis} = \Delta(y) \tau^y \sigma^y$$

which varies uniformly in the range $[-\Delta_m, \Delta_m]$ over distances comparable to the minimum coherence length $\xi_0 \sim v_F/\Delta_m$. Although this is a heuristic ansatz for an actual experimental setup, we motivate our model by noting that the leading order effect of having finite chemical potential disorder within the superconductor or near the junction and the presence of magnetic flux vortices within the superconductor cause variations in the induced pairing in the edge modes.

CAR resistance: Using the reflection coefficients, we can then find the differential conductance,

$$G(V) = \frac{dI_{exc}}{dV} = \frac{e^2}{h} (1 - |r_{ee}|^2 + |r_{he}|^2).$$

In the large bias regime, it is simplified into

$$G(eV \gg \Delta, \Gamma) \approx \frac{e^2}{h} \frac{1}{1 + Z^2},$$

similar to the regular BTK case. In the linear regime, we get

$$G(0) = \frac{2e^2}{h} \frac{1}{(1 + 2Z^2)^2},$$

which is identical to the conventional BTK, and independent of Δ . Using the fact that in this regime $I_{exc} = G(0)V$ together with $G_{XY} = e^2/h$ we arrive at

$$R_{CAR} = \frac{\hbar}{2e^2} ((1 + 2Z^2)^2 - 2),$$

which implies that $Z < Z_c = (1/\sqrt{2} - 1/2)^{1/2} \approx 0.45$ is necessary to get a negative R_{CAR} .

Now we study the $\nu = 2$ integer quantum Hall state. The edge theory is described by two chiral modes associated with the two spin degrees of freedom,

$$H_{edge} = v_F \sum_{s=\uparrow, \downarrow} \int dx \psi_s^\dagger(x) (-i\partial_x - k_{Fs}) \psi_s(x),$$

where v_F is the Fermi velocity, and $k_{F\uparrow}$ and $k_{F\downarrow}$ denote the Fermi wave vector for spin up and down.

Again, we first reduce the problem to a 1D scattering between two types of edge modes, as shown in Figure 2b (inset). Putting the two edge modes together, we write an effective Hamiltonian,

$$H_0 = v_F \sum_{s=\uparrow, \downarrow} \int dy [\psi_{Rs}^\dagger(y) (-i\partial_y - k_{Fs}) \psi_{Rs}(y) + \psi_{Ls}^\dagger(y) (i\partial_y - k_{Fs}) \psi_{Ls}(y)],$$

where we introduce two Fermi fields ψ_{Ls} and ψ_{Rs} to describe the upper and lower edge modes. Here, $s = \uparrow, \downarrow$ denotes the electron spin. We consider the proximity effect of superconductor via the following terms

$$\sum_{s=\uparrow, \downarrow} (\Delta_1 s \psi_{Rs} \psi_{L\bar{s}} + \Delta_2 \psi_{Rs} \psi_{Ls}) + \tilde{\Delta}_1 \sum_{\sigma=L,R} \psi_{\sigma\uparrow} \psi_{\sigma\downarrow} + \text{H.c.}$$

Here, Δ_1 and Δ_2 terms describe spin singlet and triplet inter-edge induced pairing while $\tilde{\Delta}_1$ describes a spin singlet intra-edge pairing, respectively. We should note that the pairing potentials Δ_1 and $\tilde{\Delta}_1$ are between spin up and down electrons while the Δ_2 pairing preserves the spin polarization. Therefore, we need spin-orbit coupling to generate the latter term as opposed to the former terms which are induced by the original s-wave pairing in the superconductor.

It is more convenient to rewrite the full Hamiltonian in the Nambu basis (Ψ_s^\dagger, Ψ_s) where $\Psi_s^\dagger = (\Psi_{RS}^\dagger, \Psi_{LS}^\dagger, \Psi_{RS}, \Psi_{LS})$. The problem can then be mapped to a single-particle BdG equation $\mathcal{H}|\Psi\rangle = E|\Psi\rangle$,

$$\mathcal{H} = v_F(-i\partial_y)\sigma_z + \sum_s k_{Fs}\tau_z|s\rangle\langle s| + \Delta_1\tau_y\sigma_x s_y + \tilde{\Delta}_1\tau_y s_y + \Delta_2\tau_y\sigma_y,$$

where $\tau_\alpha, \sigma_\alpha, s_\alpha$ are Pauli matrices acting on particle-hole, left/right mover, and spin up/down degrees of freedom, respectively. The Bogoliubov spectrum of this system for two cases of parameters is plotted in Extended Data Figure 19. Note that $\tilde{\Delta}_1$ does not open a gap in the spectrum and only shifts the zero-energy band crossings horizontally, and the gap opening between Ψ_{L1} and Ψ_{R1}^\dagger at finite energy is mediated by the s -wave induced pairing Δ_1 . It is within this energy gap that we obtain $P_h = 1$ in Extended Data Figure 19 (right panel).

To study crossed Andreev reflection, we consider a disordered pairing potential

$$V_{dis} = \Delta_1(y)\tau^y\sigma^x s^y + \Delta_2(y)\tau^y\sigma^y$$

which we vary over the minimum coherence length $\xi_0 \sim v_F/\Delta_m$. Here, both Δ_1 and Δ_2 are random variables drawn from a uniform distribution $[-\Delta_m, \Delta_m]$. The resulting CAR is shown in Extended Data Figure 20. It is evident that in both clean and disordered case the zero-bias R_{CAR} is inversely proportional to the filling ν as observed in the experiment.

FqH: Now we turn to fqH. For simplicity, we shall consider only the $\nu = 1/m$ Laughlin states (with odd m), where the edge theory is single component. The system is described by two chiral edge modes near top and bottom of the sample:

$$\mathcal{L}_{edge} = \frac{1}{4\pi\nu} \int dy [\partial_t \phi_L \partial_y \phi_L - V \partial_y \phi_L \partial_y \phi_L] + \frac{1}{4\pi\nu} \int dy [-\partial_t \phi_R \partial_y \phi_R - V \partial_y \phi_R \partial_y \phi_R]$$

where

$$[\phi_{L,R}(y_1), \phi_{L,R}(y_2)] = \mp i \frac{\pi}{m} \text{sgn}(y_1 - y_2),$$

$$[\phi_L(y_1), \phi_R(y_2)] = i \frac{\pi}{m}.$$

$\phi_{L,R}$ are chiral bosons^{49,50}. Using this formulation, the electric charge density associated with ϕ_α is given by

$$\rho_\alpha = \frac{1}{2\pi} \partial_y \phi_\alpha,$$

and the l th electron operator is described by the vertex operator

$$\Psi_{e,L/R} = e^{i\nu^{-1}\phi_{L/R}}.$$

In the right half of the system (recall Figure 2b inset) the two edge modes are decoupled. In the left half, the two edge modes are coupled via the following induced pairing term

$$\mathcal{L}_{pairing} = \Delta \int_0^\infty dx \cos \nu^{-1}(\phi_L + \phi_R).$$

Note that we drop the Klein factor since it commutes with other terms in the Hamiltonian. The bare scaling dimension of this term is $1 - \nu^{-1}$. However, we work in the strong coupling limit $\Delta \rightarrow \infty$. The ground state of the $x > 0$ region is obtained by pinning the field $\nu^{-1}(\phi_L + \phi_R) = 2\pi n$ where $n = 0, 1, 2, \dots, \nu^{-1} - 1$. This in turn implies not only $\langle e^{i\nu^{-1}(\phi_L + \phi_R)} \rangle \neq 0$ but also $\langle e^{i(\phi_L + \phi_R)} \rangle \neq 0$, that is, we get a condensate of quasi-particle and quasi-hole pairs. The scattering of a (quasi)particle impinging on the $x > 0$ region from the left region can be addressed by the following two processes:

1. Coherent conversion of a right-moving quasi-electron to a left-moving quasi-hole, which is described by the following term

$$\Gamma_{qp} \int dy \delta(y - 0^-) e^{i(\phi_L + \phi_R)} + \text{H.c.}$$

2. Coherent conversion of a right-moving electron to a left-moving hole, which is described by the following term

$$\Gamma_{eh} \int dy \delta(y - 0^-) e^{i\nu^{-1}(\phi_L + \phi_R)} + \text{H.c.}$$

The latter process requires electron bunching before going through the superconductor. The scaling dimensions of the two processes are given by ν and ν^{-1} , respectively. Hence, the tunneling amplitudes obey the renormalization flow equations

$$\frac{d\Gamma_{qp}}{dl} = (1 - \nu),$$

$$\frac{d\Gamma_{eh}}{dl} = (1 - \nu^{-1}),$$

which implies that in the infra-red limit (low energy), for $\nu < 1$, Γ_{qp} is relevant while Γ_{eh} is irrelevant. Now, we compare experimental consequences of both processes (Extended Data Figure 21):

1. Γ_{qp} : Since this term is relevant, it drives the system to a strong coupling limit fixed point $\Gamma_{qp} \rightarrow \infty$ in the low-energy limit. So, we expect that at low temperatures there is a constant CAR response proportional to $|\Gamma_{qp}|^2$ and it gradually decreases as temperature is increased $T^{2\nu-2}$ or we apply a bias voltage, $V^{2\nu-2}$.
2. Γ_{eh} : Since this term is irrelevant, at zero temperature the system in a weak coupling limit $\Gamma_{eh} \rightarrow 0$ and there is no CAR response. We expect that as we increase the temperature or apply a bias voltage, the CAR response increases as $T^{2\nu^{-1}-2}$ or $V^{2\nu^{-1}-2}$, respectively.

Given that the experimental data as a function of temperature shows an initial plateau and gradual increase as T is decreased, we conclude that Γ_{qp} is the dominant term governing the CAR response.

38. Wang, L. *et al.* One-dimensional electrical contact to a two-dimensional material. *Science* **342**, 614–617 (2013).
39. Purdie, D. G. *et al.* Cleaning interfaces in layered materials heterostructures. *Nat. Commun.* **9**, 5387 (2018).
40. Abanin, D. A., Lee, P. A. & Levitov, L. S. Charge and spin transport at the quantum Hall edge of graphene. *Solid State Commun.* **143**, 77–85 (2007).
41. Beenakker, C. W. J. Colloquium: Andreev reflection and Klein tunneling in graphene. *Rev. Mod. Phys.* **80**, 1337 (2008).
42. Cayssol, J. Crossed Andreev reflection in a graphene bipolar transistor. *Phys. Rev. Lett.* **100**, 147001 (2008).
43. Hoppe, H., Zülicke, U. & Schön, G. Andreev reflection in strong magnetic fields. *Phys. Rev. Lett.* **84**, 1804 (2000).
44. Min, H. *et al.* Intrinsic and Rashba spin-orbit interactions in graphene sheets. *Phys. Rev. B* **74**, 165310 (2006).
45. Ryu, S., Schnyder, A. P., Furusaki, A. & Ludwig, A. W. W. Topological insulators and superconductors: tenfold way and dimensional hierarchy. *New J. Phys.* **12**, 065010 (2010).
46. Schnyder, A. P., Ryu, S., Furusaki, A. & Ludwig, A. W. W. Classification of topological insulators and superconductors in three spatial dimensions. *Phys. Rev. B* **78**, 195125 (2008).
47. Kitaev, A. Y. Periodic table for topological insulators and superconductors. *AIP Conf. Proc.* **1134**, 22–30 (2009).
48. Deutscher, G. & Nozières, P. Cancellation of quasiparticle mass enhancement in the conductance of point contacts. *Phys. Rev. B* **50**, 13557 (1994).
49. Wen, X.-G. Chiral Luttinger liquid and the edge excitations in the fractional quantum Hall states. *Phys. Rev. B* **41**, 12838 (1990).
50. Wen, X.-G. Theory of the edge states in fractional quantum Hall effects. *Int. J. Mod. Phys. B* **6**, 1711–1762 (1992).

Acknowledgements We thank Gil-Ho Lee and Yuval Oreg for helpful discussions. Ö.G. acknowledges support by a Rubicon grant of the Netherlands Organization for Scientific Research (NWO). Y.R. and P.K. acknowledge support from DOE (DE-SC0012260) for measurement and analysis, and NSF (QII-TAQ5 MPS 1936263) for characterization. S.Y.L. and Y.H.L. acknowledge support from the Institute for Basic Science (IBS-R011-D1). H.S. and A.V. acknowledge support by the Simons Collaboration on Ultra-Quantum Matter, which is a grant from the Simons Foundation (651440, A.V.). J.Z. and A.Y. acknowledge support from DOE (DE-SC0019300) for device fabrication; A.Y. also acknowledges funding by the NSF DMR-1708688. P.K. and A.Y. acknowledge experimental collaboration support from Science and Technology Center for Integrated Quantum Materials, NSF Grant No. DMR-1231319. K.W. and T.T. acknowledge support from the Elemental Strategy Initiative conducted by the MEXT, Japan, Grant Number JPMXP0112101001, JSPS KAKENHI Grant Number JP20H00354 and the CREST (JPMJCR15F3). Nanofabrication was performed at the Center for Nanoscale Systems at Harvard, supported in part by an NSF NNIN award ECS-00335765.

Author contributions Ö.G., Y.R. and P.K. conceived the idea and designed the project. P.K. supervised the project. Ö.G., Y.R., S.Y.L. and J.Z. fabricated the devices. H.S. and A.V. setup the theoretical model. Y.H.L. and A.Y. consulted on and helped in different stages of the fabrication process and analysis. Ö.G., Y.R. and J.Z. performed the measurements. Ö.G., Y.R., H.S., J.Z., A.Y. and P.K. wrote the paper with inputs from all authors.

Competing interests The authors declare no competing interests.

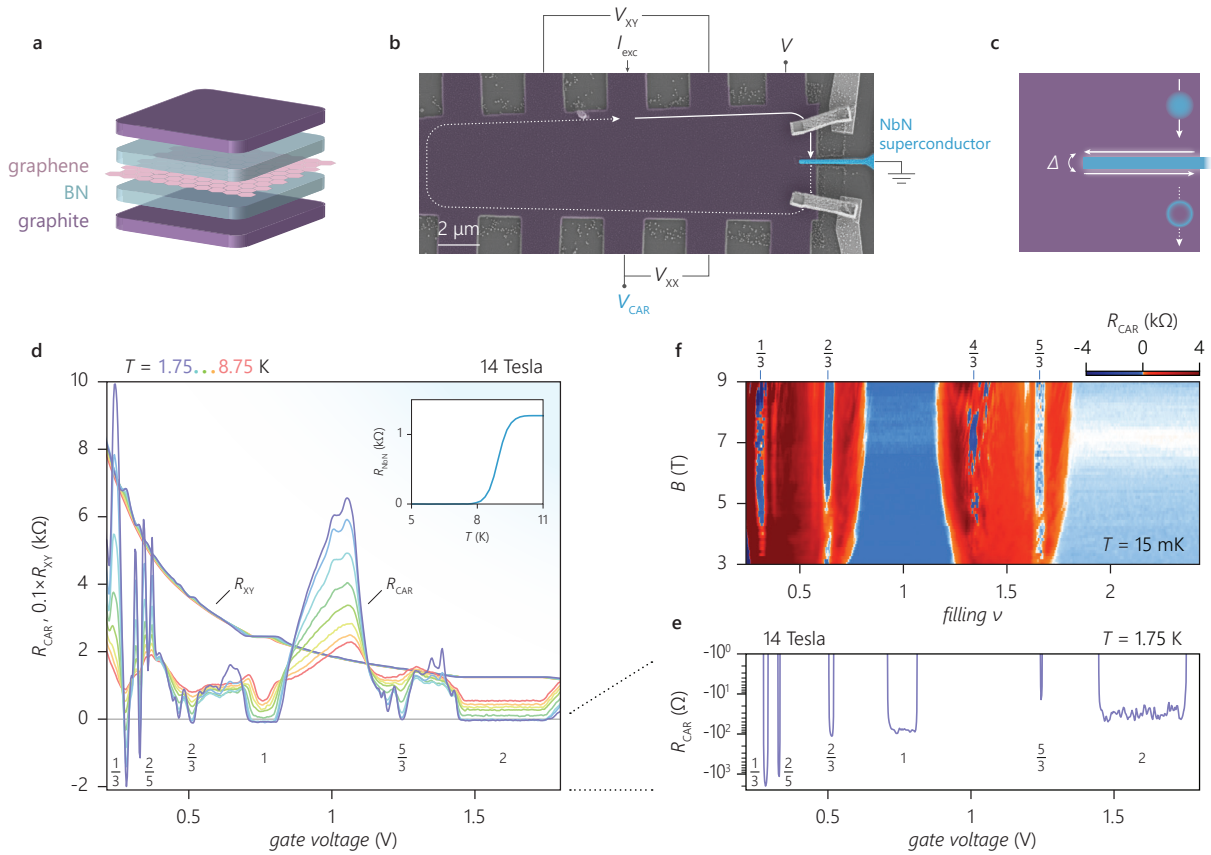


Figure 1 | Induced superconductivity in the fractional quantum Hall edge. **a**, Schematic of the heterostructure. Graphene is encapsulated with boron nitride dielectric and graphite. **b**, Typical device including a NbN superconductor ~ 100 nm in width (blue). The extended arms connect to normal leads (not shown) that are used to bias a current I_{exc} , measure the voltages V_{XX} and V_{XY} , the potential of the edge propagating towards the superconductor V , and finally that of the edge propagating away V_{CAR} . The superconductor is grounded, remaining leads are floating. The solid and the dashed arrows depict respectively the chiral electron and hole conduction in an out-of-plane magnetic field B . The metal electrodes on top graphite (gate) are bridges that

connect the top gate to leads avoiding the edge of the heterostructure. **c**, Illustration of the theory model. A narrow superconductor induces a pairing gap Δ between the counterpropagating fractional quantum Hall edges along both sides. Δ converts an incoming electron to an outgoing hole by crossed Andreev reflection (CAR). **d**, $R_{CAR} = V_{CAR}/I_{exc}$ and $R_{XY} = V_{XY}/I_{exc}$ as a function of gate voltage measured at $B = 14$ T for different temperatures T . An $R_{CAR} < 0$ at fractional quantum Hall plateaus indicates hole conductance (CAR). **Inset of d** shows the resistance of a narrow NbN for varying T which superconducts below 8 K at 14 T. **e**, R_{CAR} at 1.75 K from **d**. **f**, R_{CAR} as a function of filling ν and B measured at 15 mK. CAR ($R_{CAR} < 0$) is observed at 3 T for $\nu = 2/3$.

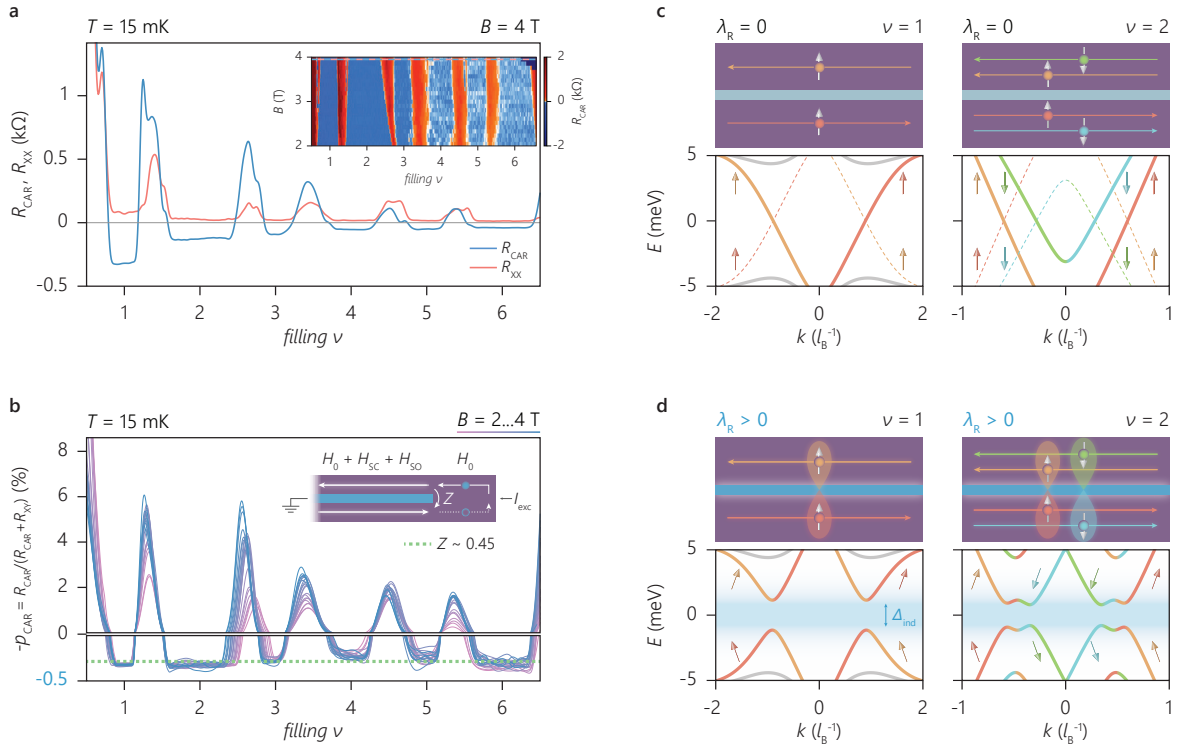


Figure 2 | Induced pairing with spin-orbit coupling. **a**, R_{CAR} and R_{XX} as a function of filling ν . All integer ν show crossed Andreev reflection (CAR, $R_{\text{CAR}} < 0$). Small R_{XX} indicates negligible bulk conductance. **Inset of a** shows R_{CAR} measured at $B = 2 \dots 4 \text{ T}$. **b**, CAR probability p_{CAR} of the **inset of a**. All integer ν , including the spin-polarized $\nu = 1$, have a comparable p_{CAR} , an evidence for the pairing mechanism being the same for all integer ν , enabled by spin-orbit coupling. The dashed line is the p_{CAR} when incoming charges can tunnel to the outgoing edge without Andreev reflection, represented by Z , shown in **inset**. $Z \sim 0.45$ matches the measurement. H_0 is the Hamiltonian of the edges, H_{SC} the pairing, and H_{SO} the spin-orbit Hamiltonian. **c**, Illustration of the edges separated by a superconductor without spin-orbit coupling ($\lambda_{\text{R}} = 0$) for $\nu = 1, 2$,

and their calculated Bogoliubov-de Gennes spectrum. No pairing gap is present ($\Delta_{\text{ind}} = 0$). Momentum k in units of l_B^{-1} with l_B the magnetic length. Solid lines are the electron-like excitations, dashed lines the hole-like. Color code indicates the spin and the direction of propagation. **d**, Inclusion of spin-orbit coupling tilts the spins and enables a pairing gap Δ_{ind} . The only possible pairing is p-wave for any integer ν irrespective of whether it is spin-polarized or not. The inner edges pair more strongly due to their proximity to the superconductor. However, for small energy and temperature, p_{CAR} is independent of the size of Δ_{ind} , a result of resonant Andreev reflection owing to the induced topological gap Δ_{ind} (quantized Majorana conductance).

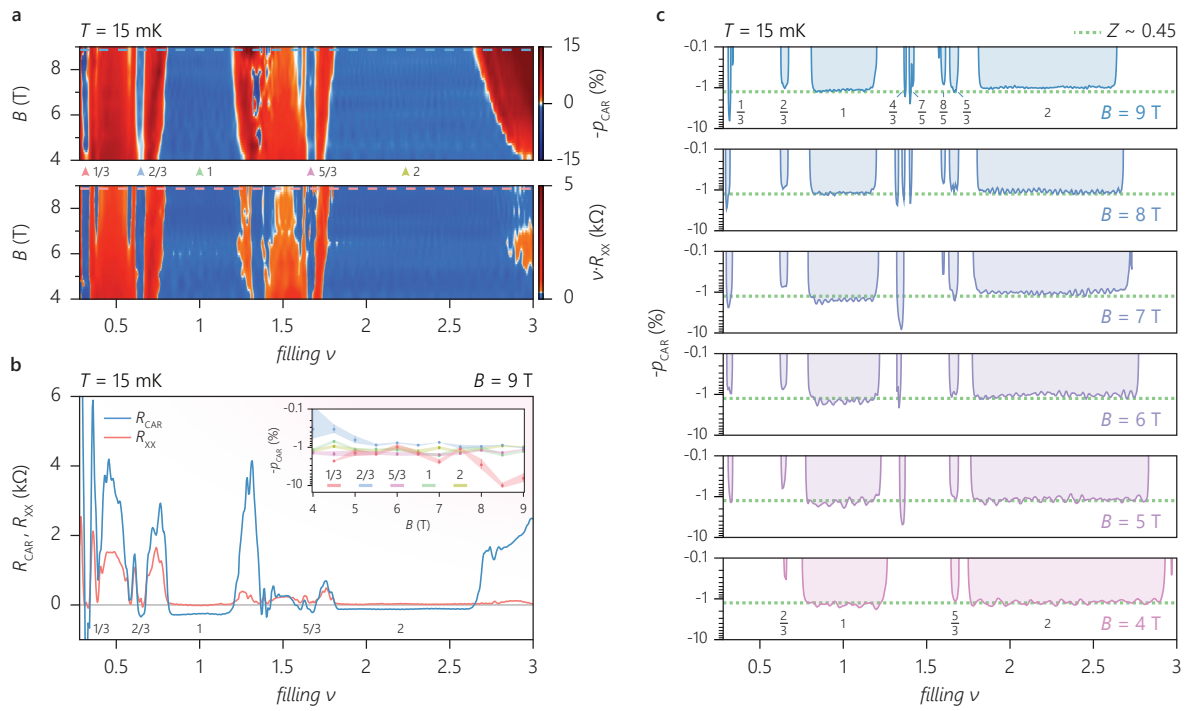


Figure 3 | Magnetic field dependence. a, p_{CAR} and R_{XX} (normalized for different ν) as a function of filling and magnetic field B . b, R_{CAR} and R_{XX} at $B=9$ T from a. Small R_{XX} indicates negligible bulk conductance. Inset of b shows p_{CAR} from a as function of B for several ν . p_{CAR} of $\nu=1/3$ shows a strong B dependence reaching 10% at $B=8.5$ T. $p_{CAR} \sim 1\%$ for the rest of the fillings shown. The shades

represent the uncertainty in the measured values. c, p_{CAR} from a for $B=4\dots 9$ T. p_{CAR} at $\nu=1/3$ and $4/3$ changes with B , reaching respectively $>6\%$ ($B=9$ T) and $>8\%$ ($B=7$ T). The rest of the fillings are insensitive to B once they are well developed. $Z \sim 0.45$ matches the measurement for fillings which do not exhibit a B dependence.

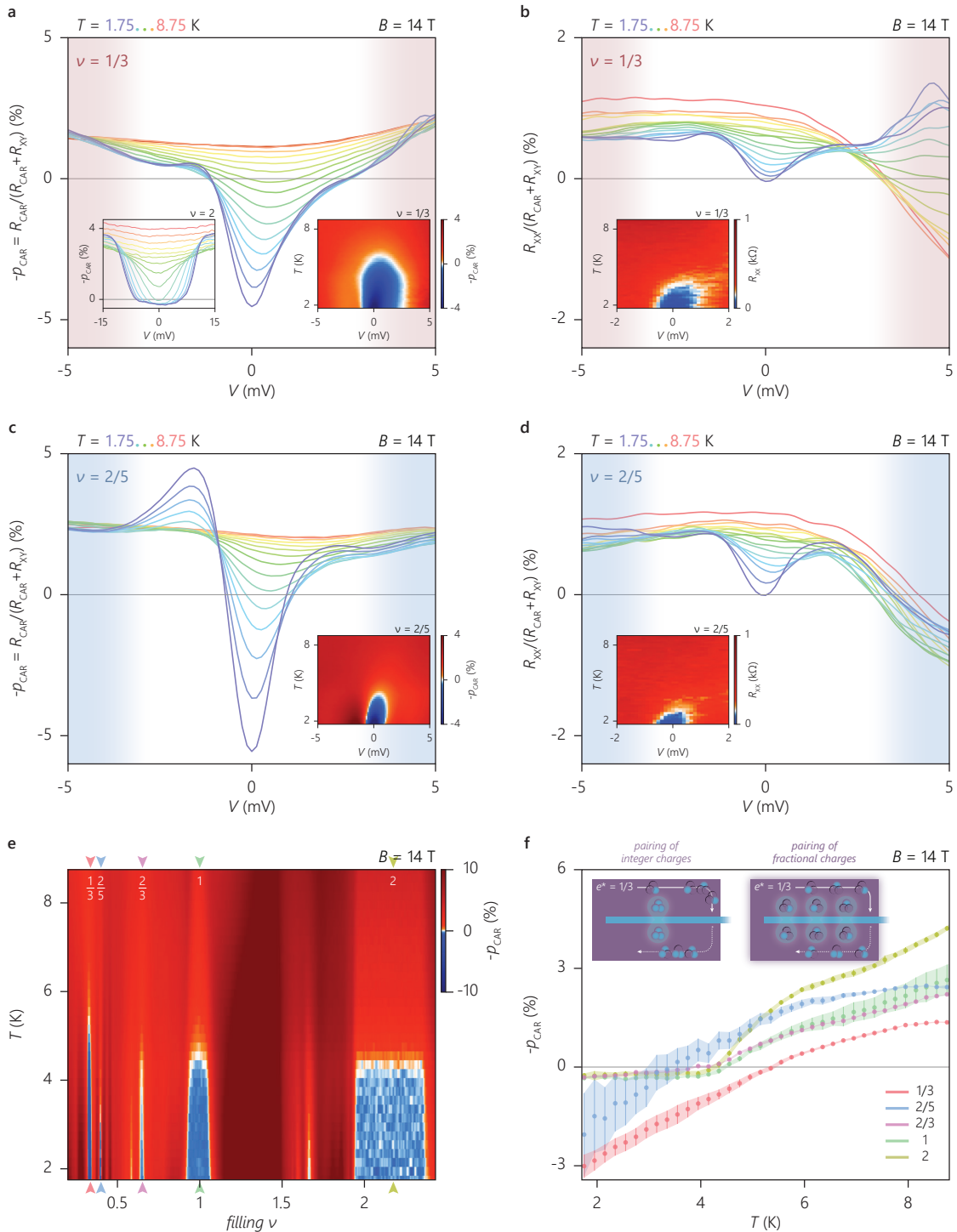
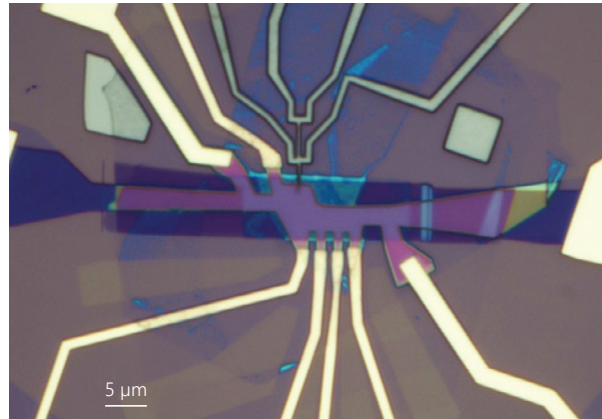


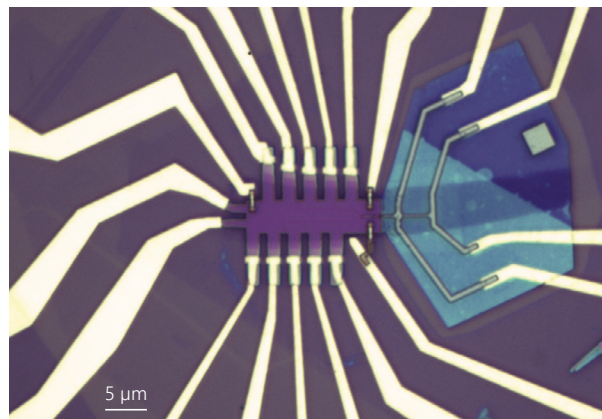
Figure 4 | Transport spectroscopy and temperature dependence. **a**, p_{CAR} at $\nu=1/3$ as a function of the incoming edge potential V (excitation) for different temperatures T . Crossed Andreev reflection (CAR) is limited to below $|eV| \sim 1$ meV and $T < 6$ K. Increasing excitation and T suppress CAR. **Left inset of a** shows p_{CAR} at $\nu=2$ with a V and T dependence similar to that at $\nu=1/3$ apart from a larger V range and a smaller p_{CAR} . **Right inset of a** shows the p_{CAR} corresponding to **a**. **b**, R_{XX} corresponding to **a**, divided by the incoming edge potential $R_{\text{CAR}}+R_{\text{XY}}$, allowing a direct comparison to p_{CAR} . Increasing excitation and T result in bulk conductance which suppresses CAR. **Inset of b** shows R_{XX} corresponding to the **right inset of a**. **c**, **d**, Same as **a** and **b** but for $\nu=2/5$ which shows a V and T dependence similar to that for $\nu=1/3$. **e**, p_{CAR} as a function of ν for varying T . $R_{\text{CAR}} < 0$ below ~ 5 K for all well-developed fillings

(highlighted with arrows). **f**, Vertical cuts from **e**. At $\nu=2/3$, 1, and 2 p_{CAR} saturates below ~ 4 K with decreasing T , whereas at $\nu=1/3$ and $2/5$ continues to increase in amplitude without saturating. The shades represent the uncertainty in the measured p_{CAR} . **Inset of f** illustrates two different mechanisms of charge transport to the superconductor. Left schematic illustrates bunching of fractional charges of $e^*=1/3$ to form integer charges of e that pair. This mechanism converts three incoming e^* to an outgoing $-e$, an integer-charged hole, adding $2e$ to the superconductor. Right schematic illustrates the pairing of fractional charges, a mechanism that converts e^* to $-e^*$, adding $2e/3$ to a topological superconductor with parafermions. For pairing of integer charges, p_{CAR} vanishes at $T=0$. In contrast, p_{CAR} monotonically increases in amplitude with decreasing T when fractional charges pair.

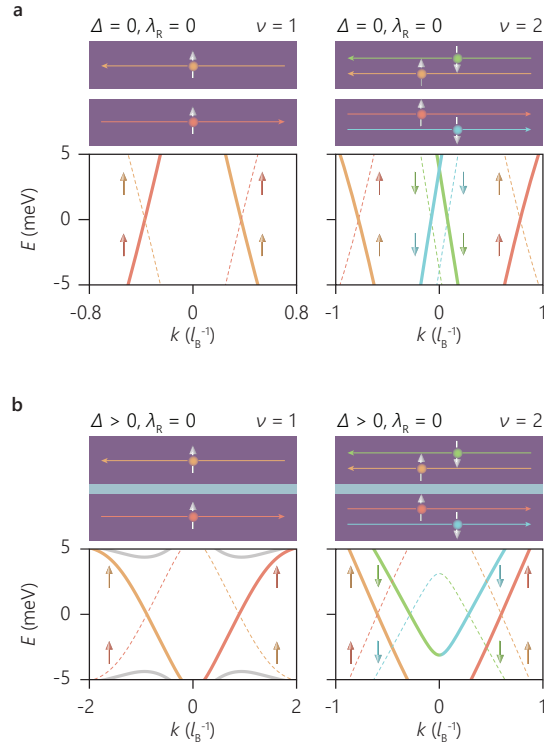
Device 1



Device 2

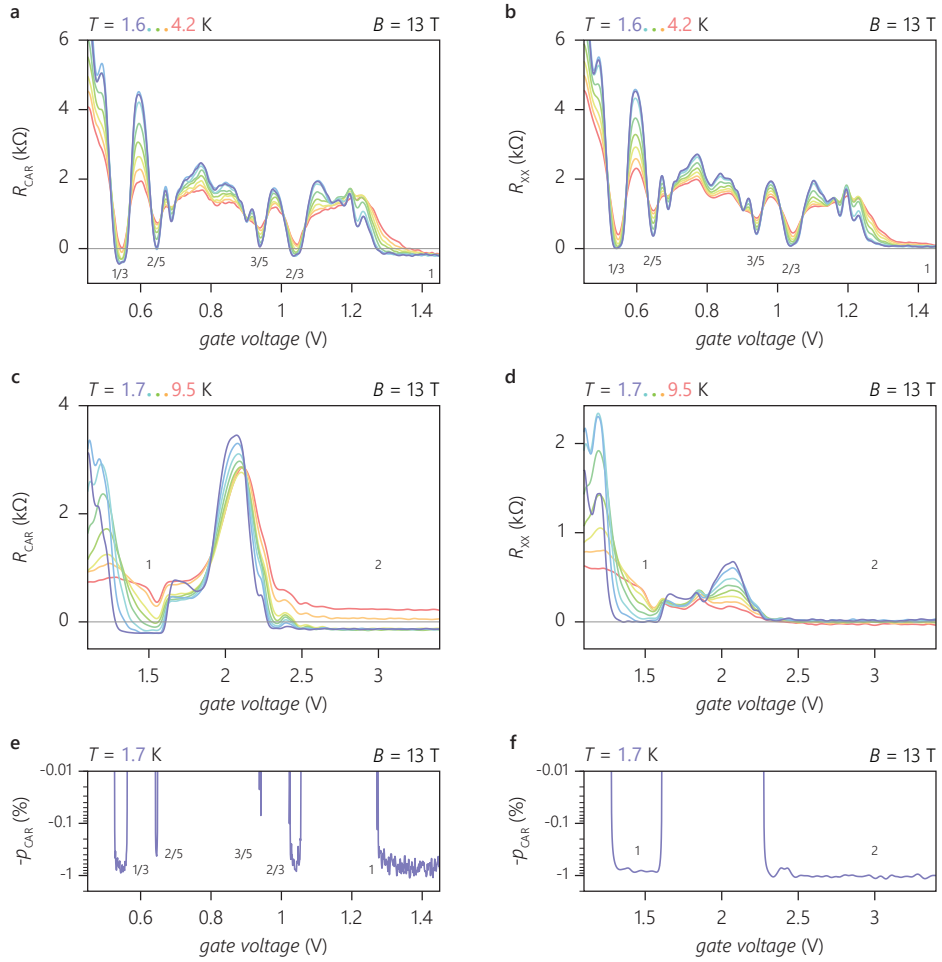


Extended Data Figure 1 | The measured devices. All data presented in the main text Figures are taken from Device 1. Data from Device 2 are presented in Extended Data Figures 3-9.



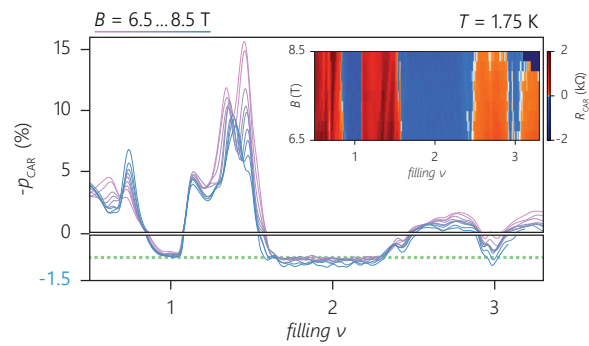
Extended Data Figure 2 | Evolution of Bogoliubov-de Gennes spectrum when including superconductivity without spin-orbit coupling. **a**, Illustration of the edges separated by vacuum for $\nu=1, 2$, and their calculated Bogoliubov-de Gennes spectrum. Momentum k in units of l_B^{-1} with l_B the magnetic length. Spectrum is doubled to show both electron-like (solid lines) and hole-like (dashed lines) excitations. Color code indicates the spin and the direction of propagation. **b**, Inclusion of superconductivity ($\Delta > 0$) without spin-orbit coupling ($\lambda_R=0$) does not affect the spin-polarization. This leaves the zero-

energy crossings spin polarized which cannot be gapped by an s-wave superconductor—an induced pairing gap Δ_{ind} does not open. **b** same as main text Figure 2c. For these simulations and the ones presented in the main text Figure 2, the system parameters are set as follows: $\Delta_1 = 0.3\epsilon_0, \Delta_2 = 0.2\epsilon_0$ ($\Delta_{1,2} = 0$ for vacuum), $m_s = 3\epsilon_0, m_n = 0.06\epsilon_0, \mu_s = 8\epsilon_0$ ($\mu_s = 0$ for vacuum), $\mu_n = 0.2\epsilon_0$ (for $\nu = 1$), $\mu_n = 0.45\epsilon_0$ (for $\nu = 2$), $g_n = 0.2\epsilon_0, \lambda_{Ry} = \lambda_{SO} = 0$ and $\lambda_{Rx} = 0.2\epsilon_0$ ($\lambda_{Rx} = 0$ for no spin-orbit), $W_s = 6l_B = 1.7\xi_0 = 62.7$ nm, $\epsilon_0 = 89$ meV.



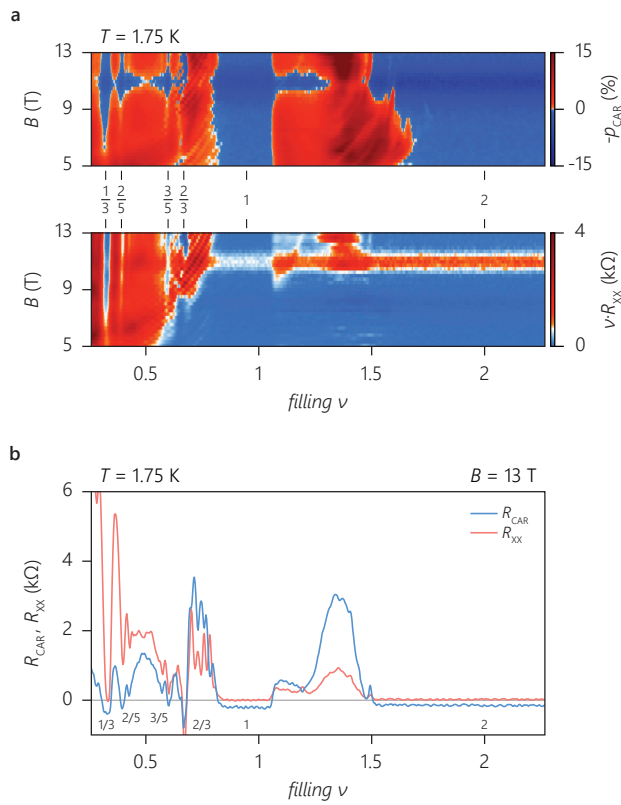
Extended Data Figure 3 | Induced superconductivity in the fractional quantum Hall edge in Device 2. a, b, R_{CAR} and R_{xx} as a function of gate voltage at $B=13$ T for different temperatures T . $R_{CAR} < 0$ at the highlighted fillings

indicates crossed Andreev reflection (CAR). c, d, same as a and b but for integer fillings 1 and 2 in a larger T range. e, f, p_{CAR} at $T=1.7$ K respectively from a and c.



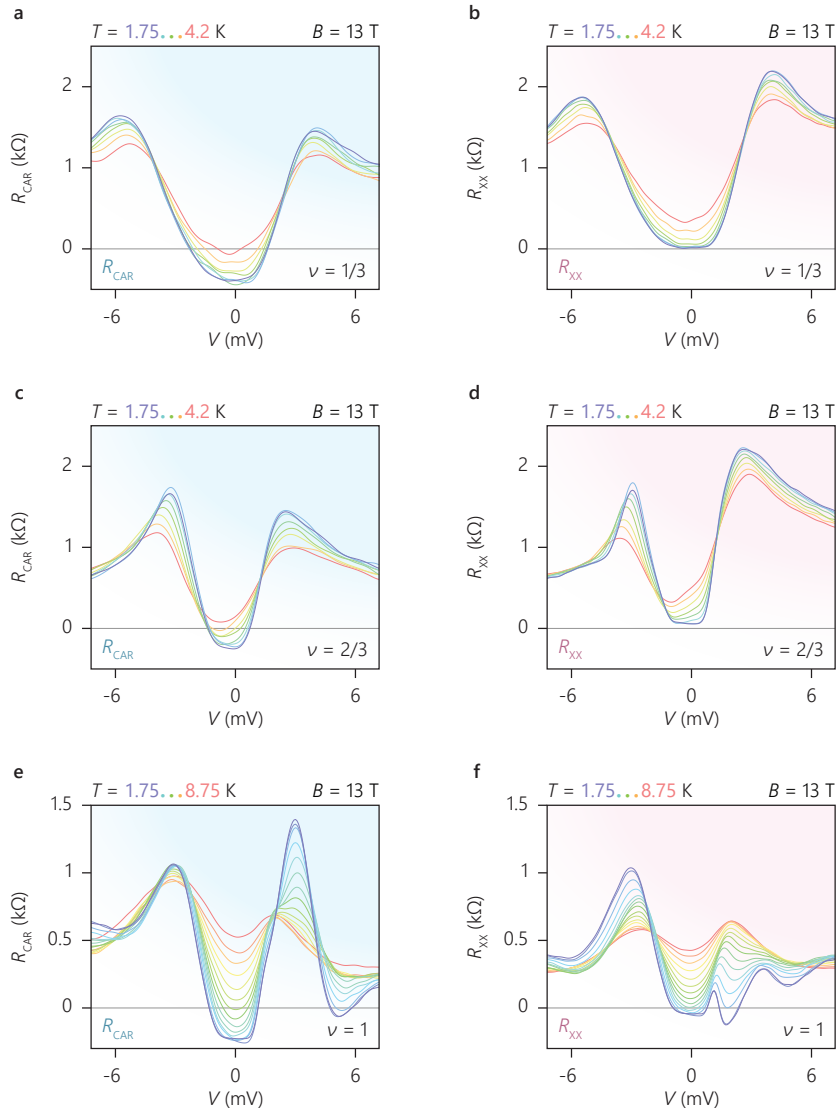
Extended Data Figure 4 | Induced pairing with spin-orbit coupling in Device 2. **a**, p_{CAR} as a function of filling ν . Integer fillings, including the spin-polarized $\nu=1$, have a comparable p_{CAR} , an evidence for the pairing mechanism enabled by spin-orbit coupling. The dashed line is the p_{CAR} expected for $Z \sim 0.45$. Inset

shows R_{CAR} measured at $B=6.5 \dots 8.5$ T. The filling axis has been adjusted such that the measured fillings align with the integer values of the axis. This procedure to convert gate voltage to filling is present in this Figure and in the main text Figure 2a and b.



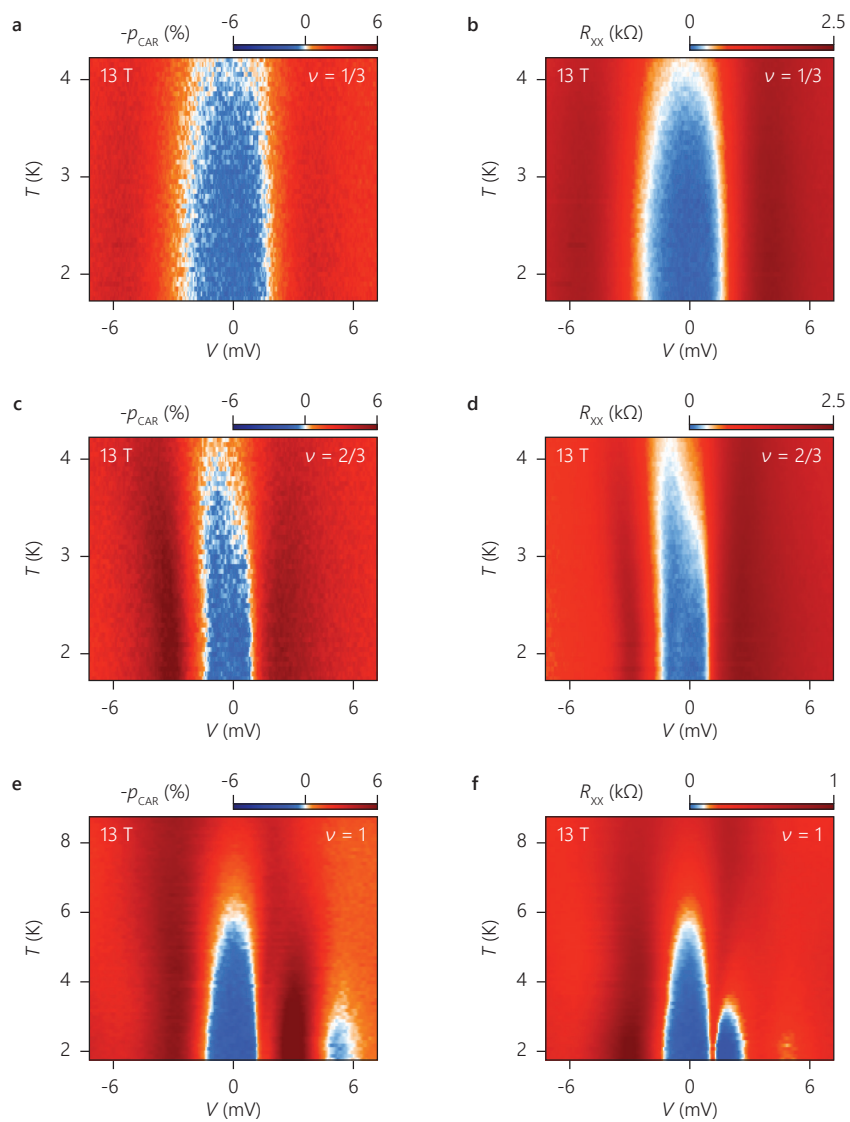
Extended Data Figure 5 | Magnetic field dependence in Device 2. a, p_{CAR} and R_{XX} (normalized for different ν) as a function of filling and magnetic field B . Crossed Andreev reflection (CAR, $R_{CAR} < 0$) is seen for all well-developed ν . Bulk conduction suppresses CAR observed for lower values of B or for fractional ν

with smaller excitation gaps. **b,** R_{CAR} and R_{XX} at $B = 13$ T from a. Bulk conduction (R_{XX}) is negligible for all highlighted fillings except $\nu = 2/3$, a complication related to equilibration in the contact, which is limited to this measurement.



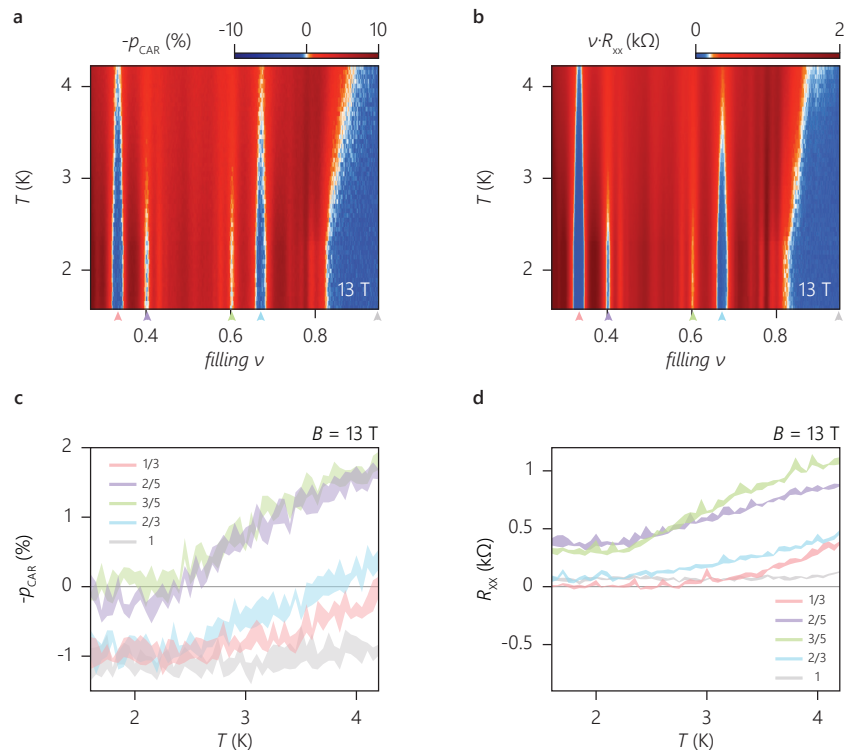
Extended Data Figure 6 | Transport spectroscopy in Device 2 (part 1). a-f, R_{CAR} and R_{XX} at several fillings as a function of the incoming edge potential V (excitation) for different temperatures T . Crossed Andreev reflection (CAR,

$R_{CAR} < 0$) is limited to below $|eV| \sim 1$ meV. Increasing excitation and T suppress CAR by increasing bulk conductance for these fillings in this device.



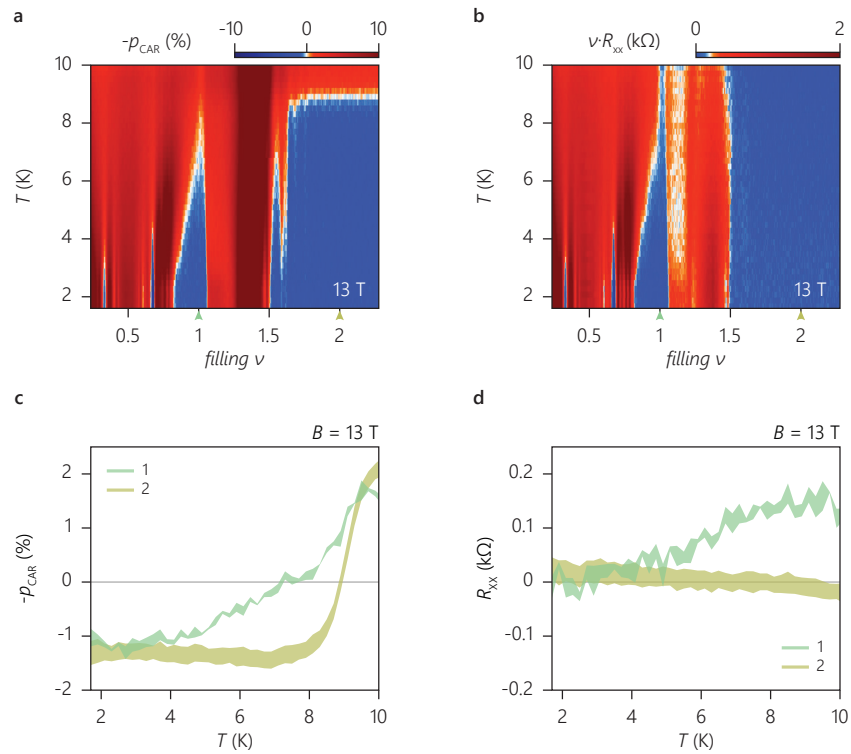
Extended Data Figure 7 | Transport spectroscopy in Device 2 (part 2). a-f, p_{CAR} and R_{xx} at several fillings as a function of the incoming edge potential V (excitation) for different temperatures T . Crossed Andreev reflection (CAR,

$R_{CAR} < 0$) is limited to below $|eV| \sim 1$ meV, $T \sim 4$ K for $\nu = 1/3$ and $2/3$, and $T \sim 6$ K for $\nu = 1$.



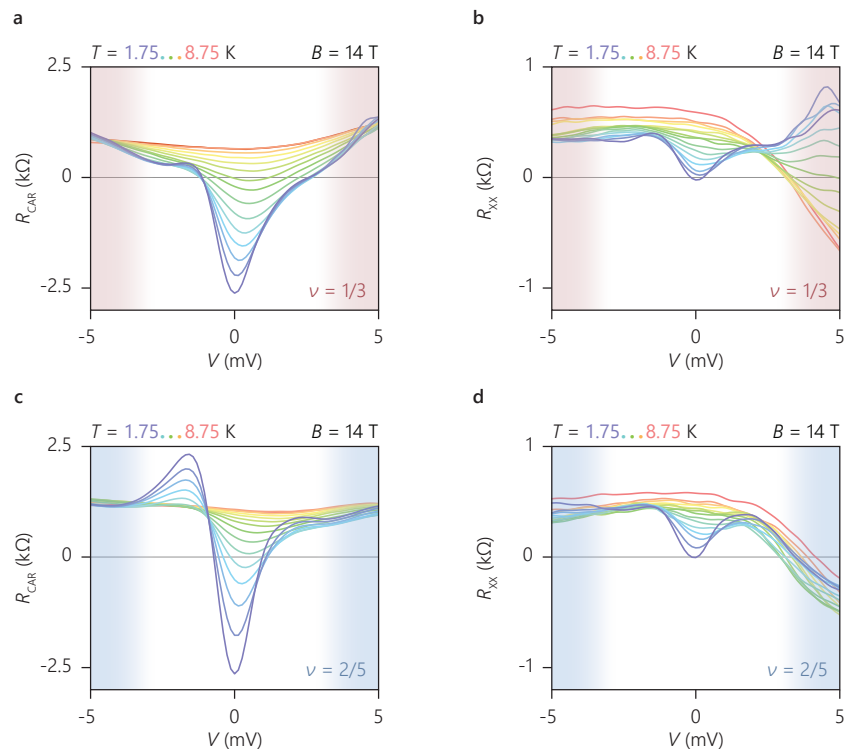
Extended Data Figure 8 | Temperature dependence in Device 2 (part 1, fractional fillings). a, b, p_{CAR} and R_{xx} (normalized for different ν) as a function of filling for varying T . Crossed Andreev reflection ($p_{CAR} > 0$) is seen for the well-

developed fillings $\nu = 1/3, 2/3$, and 1 , as well as the fillings with smaller excitation gaps $\nu = 2/5$ and $3/5$, all highlighted with arrows. c, d, Vertical cuts respectively from a and b. The shades represent the standard deviation.



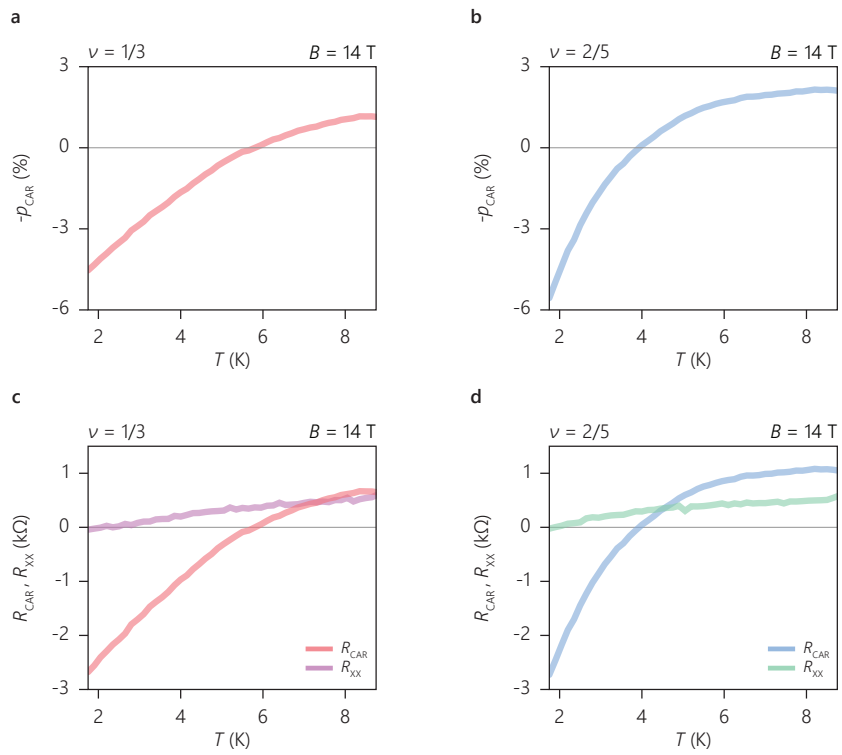
Extended Data Figure 9 | Temperature dependence in Device 2 (part 2, integer fillings). a, b, p_{CAR} and R_{xx} (normalized for different ν) as a function of filling for varying T . Crossed Andreev reflection ($p_{CAR} > 0$) is seen for both integer fillings $\nu=1$ and 2. c, d, Vertical cuts respectively from a and b. The shades

represent the standard deviation. Crossed Andreev reflection at $\nu=2$ is undisturbed by bulk conductance and suppressed when the NbN superconductor turns normal at $T \sim 9$ K.



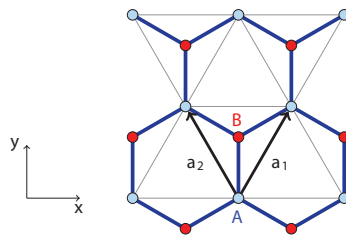
Extended Data Figure 10 | Transport spectroscopy in Device 1 showing R_{CAR} and R_{XX} . **a, b**, R_{CAR} and R_{XX} for $\nu = 1/3$ as a function of the incoming edge potential V (excitation) for different temperatures T . Crossed Andreev reflection

(CAR , $R_{CAR} < 0$) is limited to below $|eV| \sim 1$ meV. **c, d**, Same as **a** and **b** but for $\nu = 2/5$ which shows a V and T dependence similar to that for $\nu = 1/3$.



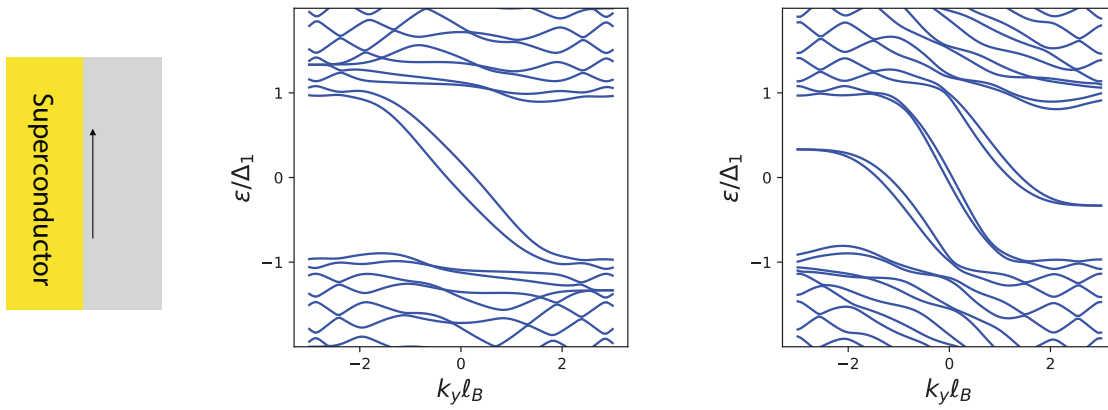
Extended Data Figure 11 | Temperature dependence of crossed Andreev reflection at $\nu=1/3$ and $2/5$ in Device 1. Probability of crossed Andreev reflection in fillings $\nu=1/3$ and $2/5$ is rapidly increasing with decreasing T down

to the lowest temperature, at which bulk conductance vanishes ($R_{XX} \sim 0$). Data extracted from main text Figure 4a-d.



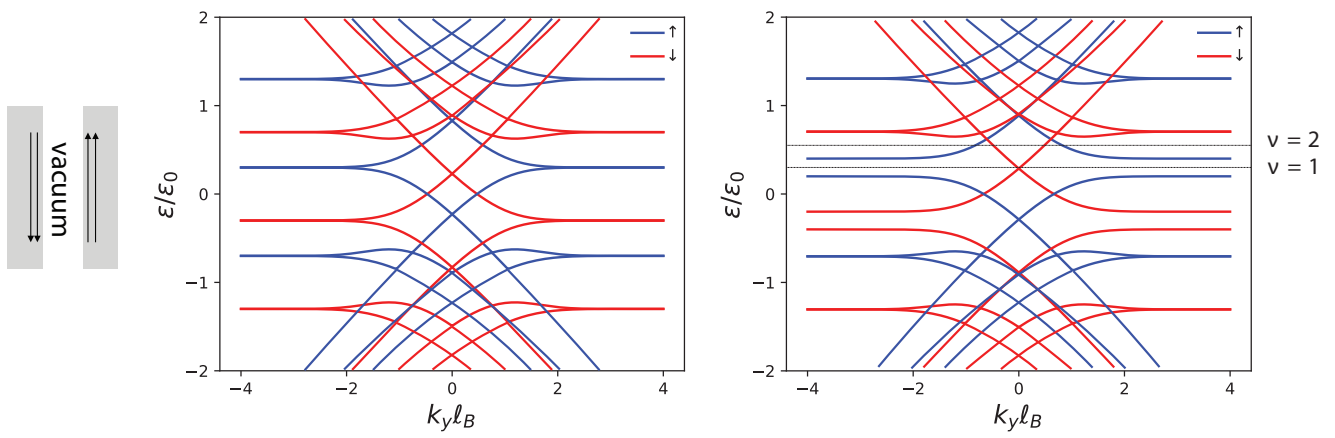
Extended Data Figure 12 | Honeycomb lattice of carbon atoms in graphene.
 Armchair and zigzag boundaries are along y and x directions, respectively.

Here, we have $\mathbf{a}_1 = a \left(\frac{1}{2} \hat{\mathbf{x}} + \frac{\sqrt{3}}{2} \hat{\mathbf{y}} \right)$, and $\mathbf{a}_2 = a \left(-\frac{1}{2} \hat{\mathbf{x}} + \frac{\sqrt{3}}{2} \hat{\mathbf{y}} \right)$ where a is the lattice constant.



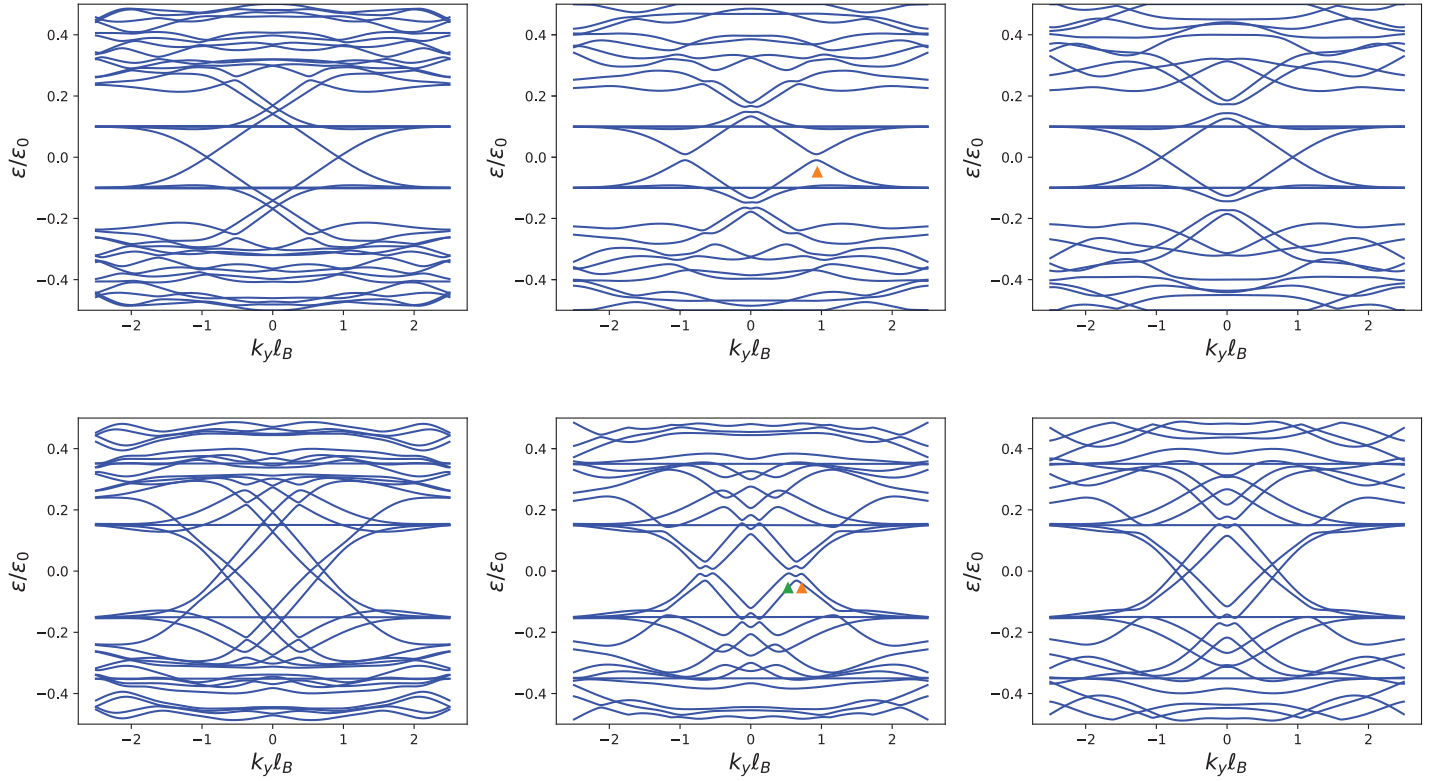
Extended Data Figure 13 | Graphene armchair edge modes near a superconductor. Plotted for the lowest two quantum Hall states $\nu = 2$ and $\nu = 6$ (this is analog of calculations in ref. 42 for graphene). Here, we set

$\Delta_1 = 0.3\epsilon_0$, $\Delta_2 = 0$, $m_s = 3\epsilon_0$, $\mu_s = 8\epsilon_0$, $m_n = 0$. We set $\mu_n = 0.4\epsilon_0$ (left) and $1.1\epsilon_0$ (right).



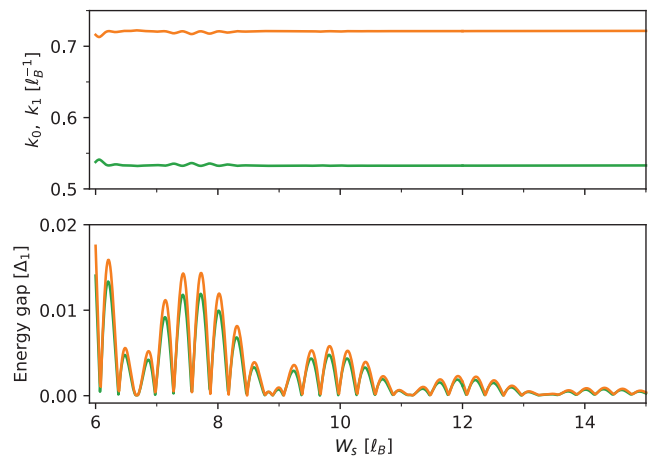
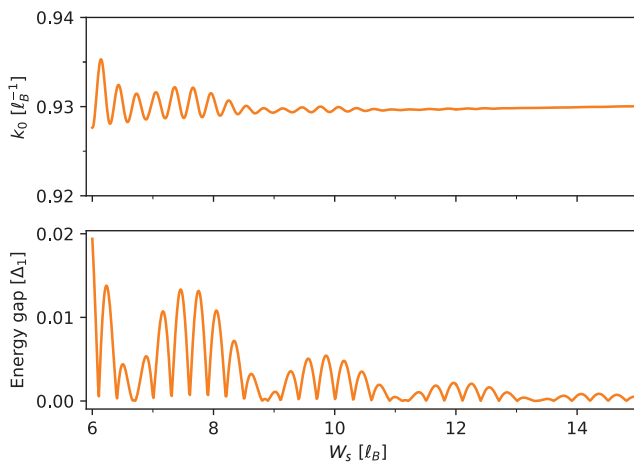
Extended Data Figure 14 | Edge modes of two half-infinite graphene quantum Hall systems separated by an insulator. Left is with, right is without inversion breaking mass term. We set the parameters for the intermediate

insulating region as $m_s = 3\epsilon_0$, $\mu_s = 0$. The width of the insulating region is $W_s = 8l_B$. For the graphene regions $\mu_n = 0$, $g = 0.3\epsilon_0$. We set $m_n = 0$ (left) and $m_n = 0.1\epsilon_0$ (right).



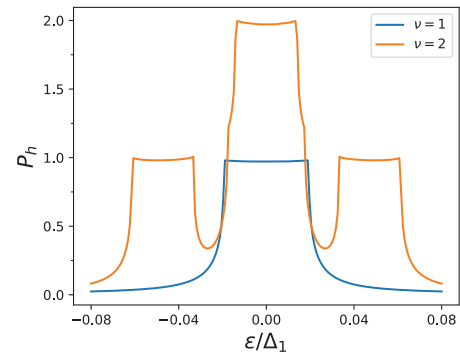
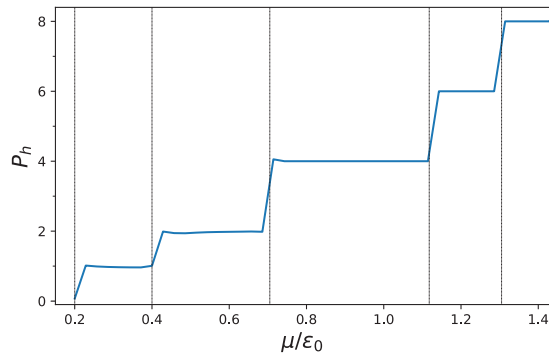
Extended Data Figure 15 | Bogoliubov spectrum. (Top row) $\nu = 1$ with $\mu_n = 0.3\epsilon_0$ and (bottom row) $\nu = 2$ with $\mu_n = 0.55\epsilon_0$ (see the right panel of Extended Data Figure 14 for the location of the chemical potential). **Left column** represents the case of a thick superconductor $W_s = 15l_B = 10\xi_0$. **Middle and right column** correspond to a thin superconductor $W_s = 6l_B = 4\xi_0$. There is no energy gap in the thick regime, while there is a gap opening in the thin regime when spin-orbit coupling is present (**middle column**). For

reference, we provide **right column** which has no spin-orbit coupling. In the other panels we set $\lambda_{Rx} = \epsilon_0$. It is evident that either turning off the spin-orbit coupling or making the superconductor thick prevent the edge modes from hybridizing and lead to a gapless spectrum with propagating Andreev edge states along the qH-superconductor interface. For these simulations, the system parameters are set as follows: $\Delta_1 = 0.5\epsilon_0$, $\Delta_2 = 0.6\epsilon_0$, $m_s = 3\epsilon_0$, $\mu_s = 8\epsilon_0$, $\lambda_{Ry} = \lambda_{SO} = 0$, $\lambda_{Rx} = \epsilon_0$.



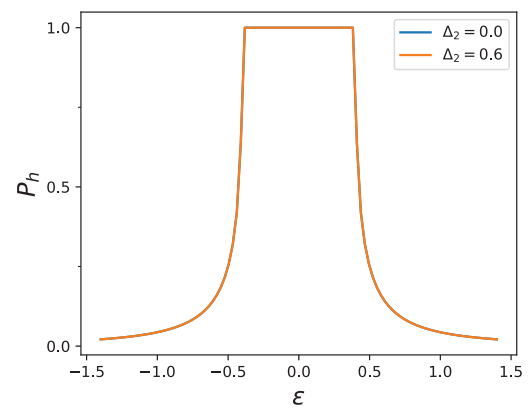
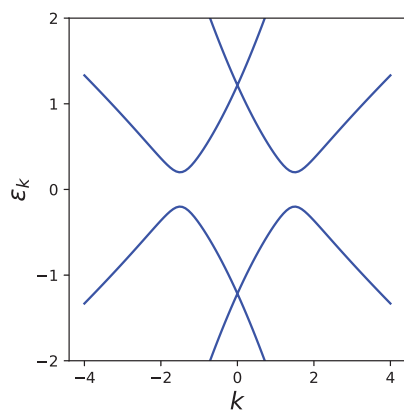
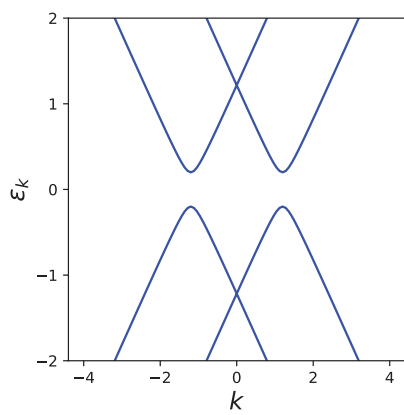
Extended Data Figure 16 | Superconductor thickness dependence. k of BdG energy minima $\pm k_0$, and $\pm k_1$ (only for $\nu = 2$), marked in the middle column of Extended Data Figure 15, and their corresponding energy gap. As the thickness

of the superconductor is increased, the gap in the BdG spectrum decreases. Other parameters are given in the Extended Data Figure 15.



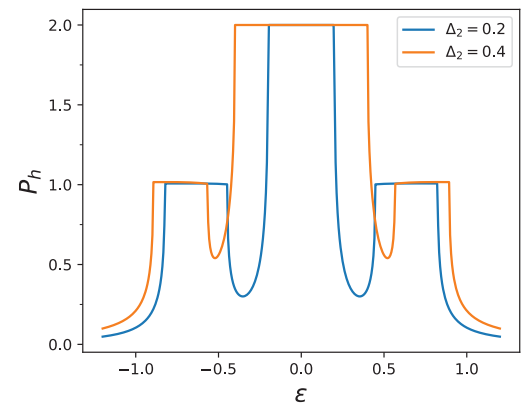
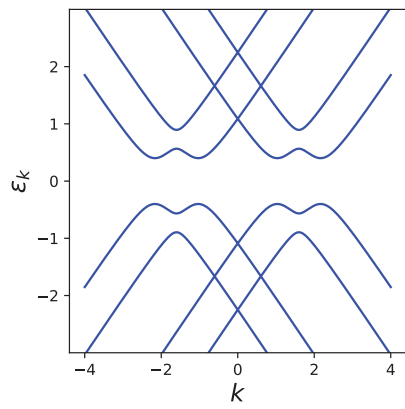
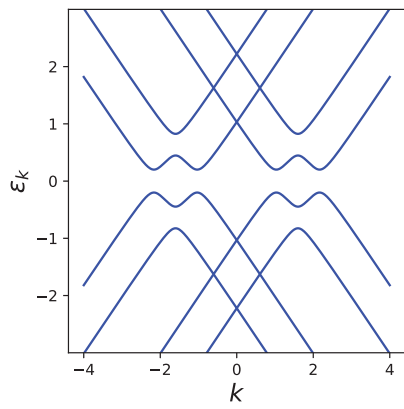
Extended Data Figure 17 | Collective probability of crossed Andreev reflection. Plotted as a function of chemical potential (left), and bias voltage

(right). Here, $W_s = 6l_B = 4\xi_0$. The rest of the parameters are given in the Extended Data Figure 15.



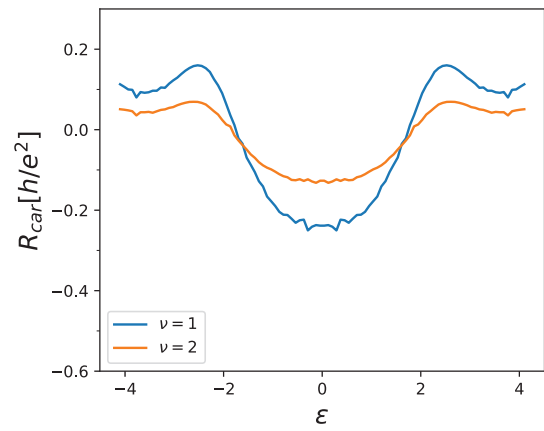
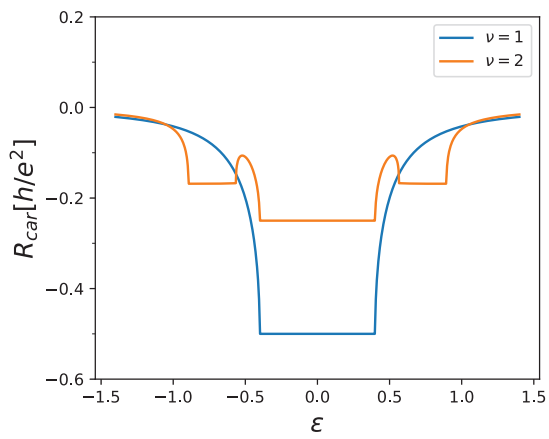
Extended Data Figure 18 | Bogoliubov spectrum at $v = 1$ edge from the effective theory. $k_0 = 1.2$, $\Delta_1 = 0.4$. We set $\tilde{\Delta} = 0$ (left) and $0.6v_F$ (middle).

Right is the collective probability of crossed Andreev reflection for the same parameters.

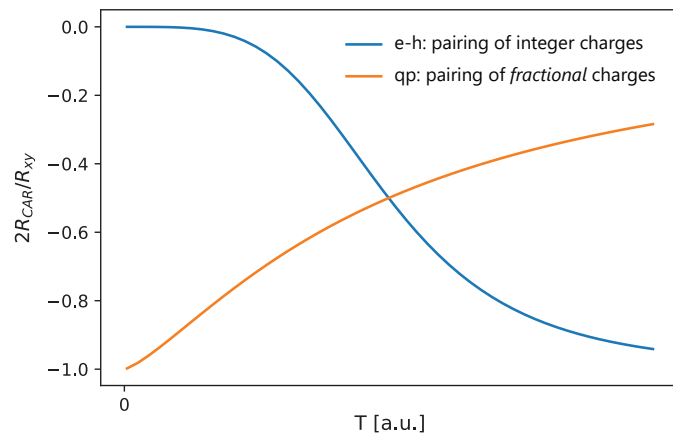


Extended Data Figure 19 | Bogoliubov spectrum at $\nu = 2$ edge from the effective theory. $k_{F1} = 2.2$, $k_{F1} = 1$, $\Delta_1 = 0.2$, $\tilde{\Delta}_1 = 0$. We set $\Delta_2 = 0.2$ (left) and

$0.4v_F$ (middle). Right is the collective probability of crossed Andreev reflection for the same parameters.



Extended Data Figure 20 | Comparison of R_{CAR} for $\nu = 1$ and 2. Left is the ideal limit, right is the disordered pairing with $Z = 0.4$.



Extended Data Figure 21 | Temperature dependence of R_{CAR} for pairing of integer and fractional charges. R_{CAR} at the edge of Laughlin states shows different temperature dependences for the two pairing scenarios.